

RESEARCH ARTICLE

10.1002/2017JA024869

Van Allen Probes Observations of Second Harmonic Poloidal Standing Alfvén Waves

Key Points:

- Second-harmonic poloidal standing Alfvén waves were observed by Van Allen Probes
- The waves were propagating westward with an azimuthal wave number of ~ 200
- Proton data exhibit signatures of bounce and drift-bounce resonances

Correspondence to:

K. Takahashi,
kazue.takahashi@jhuapl.edu

Citation:









Takahashi, K., Oimatsu, S., Nosé, M., Min, K., Claudepierre, S. G., Chan, A., ... Kim, H. (2018). Van Allen Probes observations of second-harmonic poloidal standing Alfvén waves. *Journal of Geophysical Research: Space Physics*, 123, 611–637. <https://doi.org/10.1002/2017JA024869>

Received 9 OCT 2017

Accepted 11 JAN 2018

Accepted article online 16 JAN 2018

Published online 30 JAN 2018

Kazue Takahashi¹ , Satoshi Oimatsu² , Masahito Nosé³ , Kyungguk Min¹ , Seth G. Claudepierre⁴ , Anthony Chan⁵ , John Wygant⁶ , and Hyomin Kim⁷ 

¹The Johns Hopkins University Applied Physics Laboratory, Laurel, MD, USA, ²Graduate School of Science, Kyoto University, Kyoto, Japan, ³Data Analysis Center for Geomagnetism and Space Magnetism, Graduate School of Science, Kyoto University, Kyoto, Japan, ⁴Space Sciences Department, The Aerospace Corporation, Los Angeles, CA, USA, ⁵Department of Physics and Astronomy, Rice University, Houston, TX, USA, ⁶School of Physics and Astronomy, University of Minnesota, Twin Cities, Minneapolis, MN, USA, ⁷Center for Solar-Terrestrial Research, New Jersey Institute of Technology, Newark, NJ, USA

Abstract Long-lasting second-harmonic poloidal standing Alfvén waves (P2 waves) were observed by the twin Van Allen Probes (Radiation Belt Storm Probes, or RBSP) spacecraft in the noon sector of the plasmasphere, when the spacecraft were close to the magnetic equator and had a small azimuthal separation. Oscillations of proton fluxes at the wave frequency (~ 10 mHz) were also observed in the energy (W) range 50–300 keV. Using the unique RBSP orbital configuration, we determined the phase delay of magnetic field perturbations between the spacecraft with a $2n\pi$ ambiguity. We then used finite gyroradius effects seen in the proton flux oscillations to remove the ambiguity and found that the waves were propagating westward with an azimuthal wave number (m) of ~ -200 . The phase of the proton flux oscillations relative to the radial component of the wave magnetic field progresses with W , crossing 0 (northward moving protons) or 180° (southward moving protons) at $W \sim 120$ keV. This feature is explained by drift-bounce resonance ($m\omega_d \sim \omega_b$) of ~ 120 keV protons with the waves, where ω_d and ω_b are the proton drift and bounce frequencies. At lower energies, the proton phase space density (F_{H^+}) exhibits a bump-on-tail structure with $\partial F_{H^+} / \partial W > 0$ occurring in the 1–10 keV energy range. This F_{H^+} is unstable and can excite P2 waves through bounce resonance ($\omega \sim \omega_b$), where ω is the wave frequency.

1. Introduction

Second-harmonic poloidal standing Alfvén waves, denoted P2 waves hereinafter, are among the most frequently observed ultralow-frequency (ULF) waves in the terrestrial magnetosphere. The waves are usually recognized as monochromatic oscillations in the radial component of the magnetic field (B_r) and the azimuthal component of the electric field (E_ϕ), with a frequency that falls into the Pc4 band (7–22 mHz). The first comprehensive study of P2 waves was reported by Cummings et al. (1969) based on magnetic field observations with Applications Technology Satellite (ATS)-1 placed on a geostationary orbit. Subsequent studies demonstrated that P2 waves occur in a wide range of L shells and magnetic local times (MLTs) (Anderson et al., 1990; Arthur & McPherron, 1981; Engebretson et al., 1992; Hughes & Grard, 1984; Korotova et al., 2015, 2016; Liu et al., 2013; Min et al., 2017; Schäfer et al., 2008; Singer et al., 1982; Takahashi & Anderson, 1992).

Many features of observed P2 waves can be explained by the guided poloidal mode (Cummings et al., 1969; Radoski, 1967), which is derived from the magnetohydrodynamic wave equation for a dipole magnetosphere. The mode is an idealized, purely transverse standing Alfvén wave corresponding to the limit of an infinitely large azimuthal wave number (m). The mode explains the magnetic field polarization, frequency, and magnetic latitude dependence of the amplitude and phase of the electric (\mathbf{E}) and magnetic (\mathbf{B}) field perturbations of P2 waves observed by the spacecraft (Anderson et al., 1990; Takahashi & McPherron, 1984).

In the real magnetosphere, the m number of P2 waves is finite but is still large compared to ULF waves with a strong toroidal component. According to case studies, the m value of P2 waves is of the order of 100 (Hughes et al., 1979; Le et al., 2017; Min et al., 2017; Motoba et al., 2015; Schäfer et al., 2008; Takahashi, McEntire, et al., 1990). With such m values, the wave magnetic field is undetectable on the ground because of the ionospheric

screening effect (Hughes & Southwood, 1976). Because high- m waves are unlikely to be excited by disturbances in the solar wind or on the magnetopause, instabilities in the ring current are considered to excite P2 waves.

Although numerous observations have been reported on P2 waves, there are still questions regarding their spatial properties and excitation mechanisms. To test theories for P2 wave source mechanisms, it is necessary to determine the spatial structure of the waves and gain information on the particle phase space density over a wide energy range. In this paper we present observations of a P2 wave event with the well-instrumented Van Allen Probes (also known as the Radiation Belt Storm Probes, or RBSP) spacecraft. The observations provide us with detailed information on P2 waves, including the azimuthal wave number, modulation of the flux of energetic ions, and the free energy for excitation of the waves.

The remainder of the paper is organized as follows. Section 2 presents a theoretical background. Section 3 describes the RBSP experiments. Section 4 describes the properties of the selected P2 waves. Section 5 presents signatures of proton drift-bounce resonance at ~ 100 keV. Section 6 describes wave excitation through bounce resonance of protons at 1–10 keV. Section 7 presents a summary and discussion, and section 8 presents the conclusions.

2. Theoretical Background

Theoretical studies described excitation of P2 waves through mechanisms that involve drift and bounce motions of charged particles and the finite β (plasma to magnetic field pressure ratio) effects (e.g., Cheng, 1991; Chen & Hasegawa, 1991; Cheng et al., 1994; Southwood, 1976). These studies also explain why P2 waves are more commonly excited than fundamental poloidal (P1) waves.

We consider resonant interaction of ring current ions with standing Alfvén waves as a likely mechanism for the excitation of P2 waves. This idea is justified because the waves reported in this paper were observed in the plasmasphere, where finite- β effects are not important. In a dipole magnetosphere, a particle is in resonance with a standing wave if the following condition is satisfied:

$$\omega - m\omega_d = N\omega_b, \quad (1)$$

where ω is the wave frequency, ω_d is the bounce-averaged drift frequency, and ω_b is the bounce frequency (e.g., Southwood, 1976). Both ω_d and ω_b depend on the particle velocity (denoted V), or, equivalently, energy (denoted W) and pitch angle (denoted α). For nonrelativistic cases, the approximations for ω_d and ω_b derived by Hamlin et al. (1961) for a particle moving in a dipole field are

$$\omega_b \sim \frac{\pi V}{2LR_E} \frac{1}{(1.3 - 0.56\sin\alpha_{\text{eq}})} \quad (2)$$

$$\omega_d \sim -\frac{3m_p V^2}{qB_{\text{eq}}L^2R_E^2} (0.35 + 0.15\sin\alpha_{\text{eq}}) \quad (3)$$

where q , m_p , and α_{eq} are the electric charge, mass, and equatorial pitch angle of the particle, respectively. The particle is located on magnetic field lines with geocentric distance $L R_E$ and equatorial field magnitude B_{eq} , where R_E is the radius of the Earth.

We take ω_b and the real part of ω to be positive while letting m and ω_d carry a sign. The sign of m is negative for westward propagating waves, and the sign of ω_d is negative for positively charged particles, which drift westward in Earth's dipole magnetic field. For standing waves that are purely symmetric or antisymmetric about the magnetic equator, geometric considerations require N to be an even integer for symmetric (odd) standing waves (e.g., fundamental mode) and an odd integer for antisymmetric (even) standing waves (e.g., P2 waves) (Southwood & Kivelson, 1982). Here the symmetry refers to the pattern of field line displacement, bulk velocity, or electric field about the magnetic equator. The symmetry of the transverse magnetic field perturbation is the opposite.

Figures 1a and 1b illustrate the relationship between the orbits of the guiding center of ions that are in resonance with a P2 wave and the structure of the wave electric field δE_ϕ , following Southwood and Kivelson (1982) and assuming $N = \pm 1$. The wave is assumed to be propagating westward ($m < 0$). In both figures, the wave field is captured in a frame moving azimuthally with the wave. For an ion to be in resonance with the wave, the ion needs to travel through the wave field seeing δE_ϕ of the same sign.

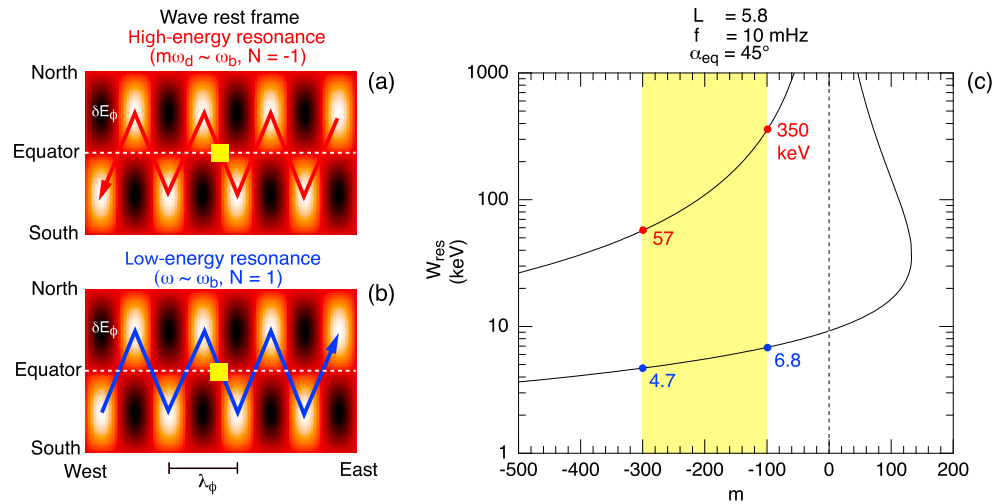


Figure 1. (a) Illustration of the guiding center orbit of a high-energy ion in resonance with a westward propagating P2 wave. The background indicates the north-south and east-west structure of the wave electric field δE_ϕ seen in a frame moving with the wave. The dark and light portions indicate negative and positive δE_ϕ values, respectively. The white dashed line indicates the magnetic equator. The zigzag line indicates the guiding center orbit of an ion mirroring at the δE_ϕ maxima. The guiding center moves westward in the wave rest frame. The yellow square indicates the location of an equatorial spacecraft. (b) Same as Figure 1a but for a low-energy ion. The guiding center moves eastward in the wave rest frame. (c) Energies of ions in resonance with a P2 wave, plotted as a function of m . A frequency and an L value representative of the observed P2 waves are used to calculate the energies, and the equatorial pitch angle is assumed to be 45° .

Resonance is possible at two energies. In the case illustrated in Figure 1a, the ion's azimuthal drift velocity is higher than the wave azimuthal phase velocity, and the resonance occurs at a high energy. An approximate solution of equation (1) for this case is $m\omega_d \sim \omega_b$ ($N = -1$), and the resonance is often referred to as high-energy resonance or drift-bounce resonance. In the case illustrated in Figure 1b, the ion's azimuthal drift velocity is lower than the wave azimuthal phase velocity, and the resonance occurs at a low energy. An approximate solution of equation (1) for this case is $\omega \sim \omega_b$ ($N = 1$), and the resonance is often referred to as low-energy resonance or bounce resonance.

We can estimate the energies of particles that are in resonance with the observed P2 waves reported here. Figure 1c shows the proton resonance energies at $L = 5.8$ as a function of m obtained by solving equations (1)–(3) for $\omega = 2\pi f_{p2}$, $N = \pm 1$, and $\alpha_{eq} = 45^\circ$, where f_{p2} is the P2 wave frequency of 10 mHz. For the m range of -300 to -100 , which corresponds to the results described in section 4, the low-energy resonance occurs in a narrow energy range 4.7–6.8 keV, while the high-energy resonance occurs in a wide energy range 57–350 keV. Note that the resonance energies depend on α_{eq} because ω_d and ω_b depend on α_{eq} differently.

Within the framework of the scenario described above, whether a particular resonance contributes to wave growth depends on the property of the ion phase space density, F . According to Southwood and Hughes (1983), the instability condition is given by

$$\frac{dF}{dW} = \left. \frac{\partial F}{\partial W} \right|_{M,L} + \left(\frac{dL}{dW} \right) \left. \frac{\partial F}{\partial L} \right|_{M,W} > 0, \quad (4)$$

where M is the magnetic moment defined by $M = W \sin^2 \alpha / B$ using the magnetic field magnitude B at the location of the particle. Equation (4) indicates that an instability occurs either from energy inversion (a bump-on-tail structure) in F (the first term on the right-hand side, r.h.s., of the equation)

$$\left. \frac{\partial F}{\partial W} \right|_{M,L} > 0 \quad (5)$$

or from a radial gradient of the phase space density (the second term on the r.h.s.)

$$\left(\frac{dL}{dW} \right) \left. \frac{\partial F}{\partial L} \right|_{M,W} > 0. \quad (6)$$

Because $dL/dW < 0$ for ions interacting with westward propagating waves (Chan, 1991, equation (2.39) and following discussion; Southwood et al., 1969), $\partial F/\partial L|_{M,W} < 0$ (inward gradient) is required for an instability.

The first type of instability (equation (5)) has been considered to drive P2 waves through bounce resonance $\omega \sim \omega_b$. A positive $\partial F/\partial W$ is very common in the ring current at energies 1–50 keV as part of a bump-on-tail energy distribution. The distribution results from ion injection on the nightside, followed by energy-dependent drift of the ions in a global-scale electric field (Baddeley et al., 2004; Chisham, 1996; Ejiri et al., 1980; Wilson et al., 2006). Spacecraft observations of simultaneous occurrence of inverted ion energy distributions and P2 waves have been taken as evidence of the bounce resonance mechanism (Hughes et al., 1978; Liu et al., 2013).

The second type of instability (equation (6)) can excite P2 waves through the high-energy (or drift-bounce) resonance $m\omega_d \sim \omega_b$ as was discussed by Takahashi, McEntire, et al. (1990) and Min et al. (2017). Takahashi, McEntire, et al. did not examine $\partial F/\partial W$ in the expected energy range of proton bounce resonance (1–10 keV), so it is not clear whether the resonance was relevant to their wave event.

A theoretical reason why P2 waves are observed more often than P1 waves (e.g., Takahashi et al., 1992) is that excitation of P1 waves through drift resonance ($m\omega_d - \omega = 0$) requires

$$\partial F/\partial L|_{M,J} < 0, \quad (7)$$

whereas excitation of P2 waves through the high-energy resonance does not (Chen & Hasegawa, 1988; Southwood, 1976), where J is the second adiabatic invariant given by $J \equiv \oint p_{\parallel} ds$. Formation of an inward gradient (equation (7)) would be an exception rather than a norm in the region $L < 7$ where P1 waves are observed (e.g., Motoba et al., 2015), because ring current ions are most likely injected from regions outside of $L = 7$, leading to $\partial F/\partial L|_{M,J} \geq 0$ at $L < 7$ under normal circumstances. Another reason is that symmetric modes (such as P1 waves) are more strongly stabilized by nonresonant bouncing particles (Chen & Hasegawa, 1991; Cheng & Qian, 1994).

3. Experiments

The RBSP spacecraft were launched on 30 August 2012 and have been on nearly identical elliptical orbits with apogee at $\sim 5.8 R_E$, a perigee altitude of ~ 600 km, an inclination of $\sim 10^\circ$, and an orbital period of ~ 9 h. The spacecraft are spin stabilized with the spin axis maintained within 27° of the Sun-Earth line (Mauk et al., 2012) and a spin period of ~ 11 s. The orbital period slightly differs between the two spacecraft, and as a result, the spacecraft were lapping at a rate of once every ~ 70 days at the time of the observations reported here. We specify the RBSP positions using the magnetic shell parameter L , magnetic latitude (MLAT), and MLT, which are defined using a centered dipole.

RBSP particle data used in this study include low-energy (< 52 keV) ion fluxes measured by the Helium Oxygen Proton Electron (HOPE) instrument (Funsten et al., 2013) and energetic (~ 50 – 300 keV) proton fluxes measured by the Magnetic Electron Ion Spectrometer (MagEIS) instrument (Blake et al., 2013), and the Radiation Belt Storm Probes Ion Composition Experiment (RBSPICE) (Mitchell et al., 2013). The two energetic ion experiments are complementary in that MagEIS provides better energy coverage with a single telescope while RBSPICE provides better directional coverage with six telescopes.

To take full advantage of particle flux measurements, it is necessary to understand the geometry of the detector look direction. Figure 2 illustrates the relationship between the look direction and the spacecraft coordinates for MagEIS and RBSPICE. The look direction of each telescope is specified by the polar angle (Θ_{look}) measured from the spacecraft spin axis, which is the Z_{SC} axis of the spacecraft body coordinates, and the azimuthal angle (Φ_{look}) about the Z_{SC} axis, measured from the X_{SC} axis (Figure 2a). The Z_{SC} axis needs to be close to the Sun-Earth line for the solar panels to get adequate illumination, but it also needs to maintain a finite angle (not exceeding 27°) from the Sun direction for the two sun sensors to detect sharp sun pulses for attitude determination. The spin phase of the spacecraft is specified by the angle Φ_{spin} (Figures 2b and 2c), which is defined to be zero when the Sun vector, the red arrow in Figure 2b, lies in the $Z_{\text{SC}}-Y_{\text{SC}}$ plane with a positive Y_{SC} component. MagEIS has a single proton telescope, whereas RBSPICE consists of six telescopes with look directions evenly spaced in the polar angle with a 10° offset from both north and south poles. Pitch angle distributions are obtained using the spacecraft rotation. With MagEIS, the pitch angle coverage depends on

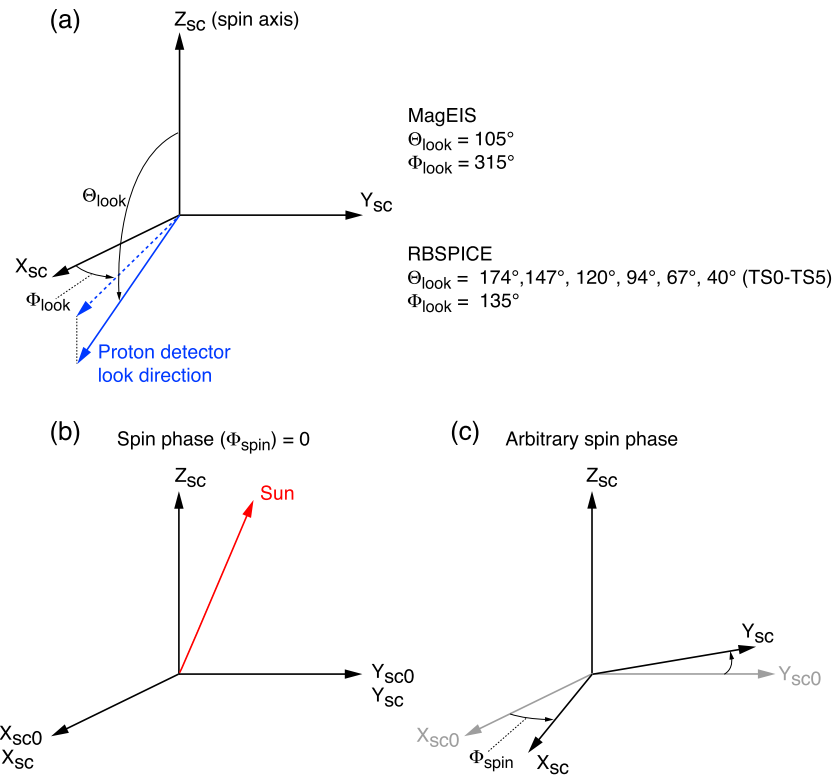


Figure 2. (a) Look direction of particle detectors in the orthogonal spacecraft (SC) body coordinates. The Z_{sc} axis is parallel to the spin axis, and the X_{sc} and Y_{sc} axes are in the spin plane. The polar (Θ_{look}) and azimuthal (Φ_{look}) angles of the look direction are given for the single telescope MaGEIS proton detector and the six-telescope RBSPICE ion detector. (b and c) Definition of the spin phase Φ_{spin} . The phase is zero when the Sun direction lies in the Y_{sc} - Z_{sc} plane and has a positive Y_{sc} component. The X_{sc} and Y_{sc} axes at zero spin phase are labeled X_{sc0} and Y_{sc0} , respectively.

the orientation of the spin axis relative to the magnetic field. With RBSPICE, nearly a full range of pitch angles is covered regardless of the magnetic field orientation by virtue of the six telescopes.

RBSP fields data used in this study include electric field vectors measured by the Electric Field and Waves Suite (EFW) experiment (Wygant et al., 2013) and magnetic field vectors measured by the Electric and Magnetic Field Instrument Suite and Integrated Science (EMFISIS) experiment (Kletzing et al., 2013). The EMFISIS experiment includes a plasma wave spectrum analyzer, which provides information on the electron number density (Kurth et al., 2015).

We use magnetic field aligned (MFA) coordinate systems for the electric (\mathbf{E}) and magnetic (\mathbf{B}) fields measured by RBSP as was done previously (Takahashi et al., 2016). In the MFA system (illustrated in Figure 3b), \mathbf{e}_μ is the direction of a reference magnetic field \mathbf{B}_{ref} . \mathbf{e}_ϕ (eastward) is in the direction of $\mathbf{e}_\mu \times \mathbf{R}$, where \mathbf{R} is the spacecraft position vector relative to the center of the Earth, and \mathbf{e}_ν (outward) completes a right-handed orthogonal system ν - ϕ - μ .

The \mathbf{E} field data are originally provided in the modified Geocentric Solar Ecliptic (MGSE) coordinates, in which \mathbf{e}_{xMGSE} (approximately sunward) is parallel to the spacecraft spin axis, \mathbf{e}_{yMGSE} (duskward) is the direction of $\mathbf{e}_{zGSE} \times \mathbf{R}$, where \mathbf{e}_{zGSE} points to the ecliptic north, and \mathbf{e}_{zMGSE} (northward, in the direction of $\mathbf{e}_{xMGSE} \times \mathbf{e}_{yMGSE}$) completes the right-handed orthogonal system x - y - z . During the observations reported here, the spin axis orientation (x, y, z) in the GSE coordinates was (0.94, 0.02, 0.34) at RBSP-A and (0.94, 0.00, 0.34) at RBSP-B, and the corresponding angle between the spin axis and the Sun-Earth line was 20° at both spacecraft. The \mathbf{E} field data used in this study were obtained in the spin plane of the spacecraft by spherical probes mounted at the end of four wire booms. The electric field measured in the rotating system is despun into the E_{yMGSE} and E_{zMGSE} components in the MGSE coordinates. The electric field component along the spin axis (E_{xMGSE}) can be estimated using the $\mathbf{E} \cdot \mathbf{B} = 0$ condition if the magnetic field elevation angle (λ_B) measured from the spin plane is not too close to zero. According to Ali et al. (2016), the threshold angle is 6° . The \mathbf{E} field vectors in the MGSE

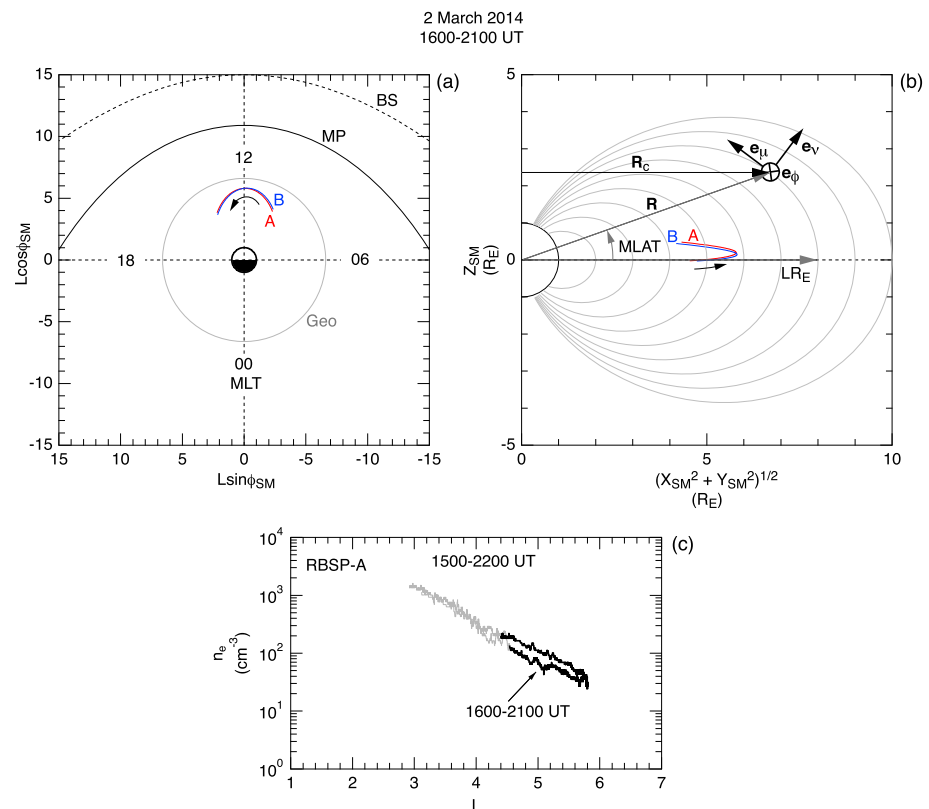


Figure 3. (a) RBSP orbit segments in L (radius) and MLT (azimuth) coordinates for the selected interval of P2 wave activity. The $L = 6.6$ circle represents geostationary orbits. (b) The same orbit segments projected onto the dipole meridian plane of the spacecraft. The MFA coordinate axes are also illustrated for a point given by the position vector \mathbf{R} on the field line that crosses the magnetic equator at $8 R_E$, where R_E is the radius of the Earth ($= 6,371.2$ km). MLAT is the magnetic latitude of the point. R_c is the radial distance in the cylindrical coordinates referenced to the Z_{SM} (dipole) axis. (c) Electron density at RBSP-A, plotted as a function of L . The heavy portion indicates the presence of P2 waves.

systems are rotated into the MFA system using the measured magnetic field as \mathbf{B}_{ref} . To express magnetic fields of observed ULF waves, we define the MFA coordinates using the T89c (Tsyganenko, 1989) model magnetic field as \mathbf{B}_{ref} instead of the running averages of the measured magnetic field (Liu et al., 2016; Zhu & Kivelson, 1991). If \mathbf{B}_{ref} is defined by the running average of the measured field, the transverse components in the MFA coordinates are high-pass filtered. This results in undesired low-frequency cutoff in the power spectra of the transverse components, which produces artificial spectral peaks just above the cutoff frequency.

4. Wave Properties

This section presents the details of the properties of the P2 waves observed at 1600–2100 UT of 2 March 2014, using field vectors and ion fluxes measured by RBSP.

4.1. Overview of the Wave Event

During the selected P2 wave event, the RBSP spacecraft were in the noon sector as illustrated in Figure 3a, where ϕ_{SM} is the azimuthal angle about the z axis of the solar magnetospheric coordinates, measured from the positive x axis. The two spacecraft had nearly identical orbits, but RBSP-B was ahead of RBSP-A by ~ 9 min. The orbit segments cover an L range of 4.4–5.8 and an MLT range of 10–14 h. Figure 3b shows that the spacecraft were close to the magnetic equator. Electron density estimated from the plasma wave spectra (Figure 3c), shown for nearly the whole orbit (1500–2200 UT), was higher than 20 cm^{-3} and indicates that the P2 waves were detected in the plasmasphere. There is no indication of a distinctive plasmasphere boundary layer, which was reported by Liu et al. (2013) in their study of P2 waves.

Figure 4 shows geomagnetic indices and RBSP-A overview plots covering the P2 wave event. The waves occurred during a period of low geomagnetic activity. The wave event was preceded by a geomagnetic storm

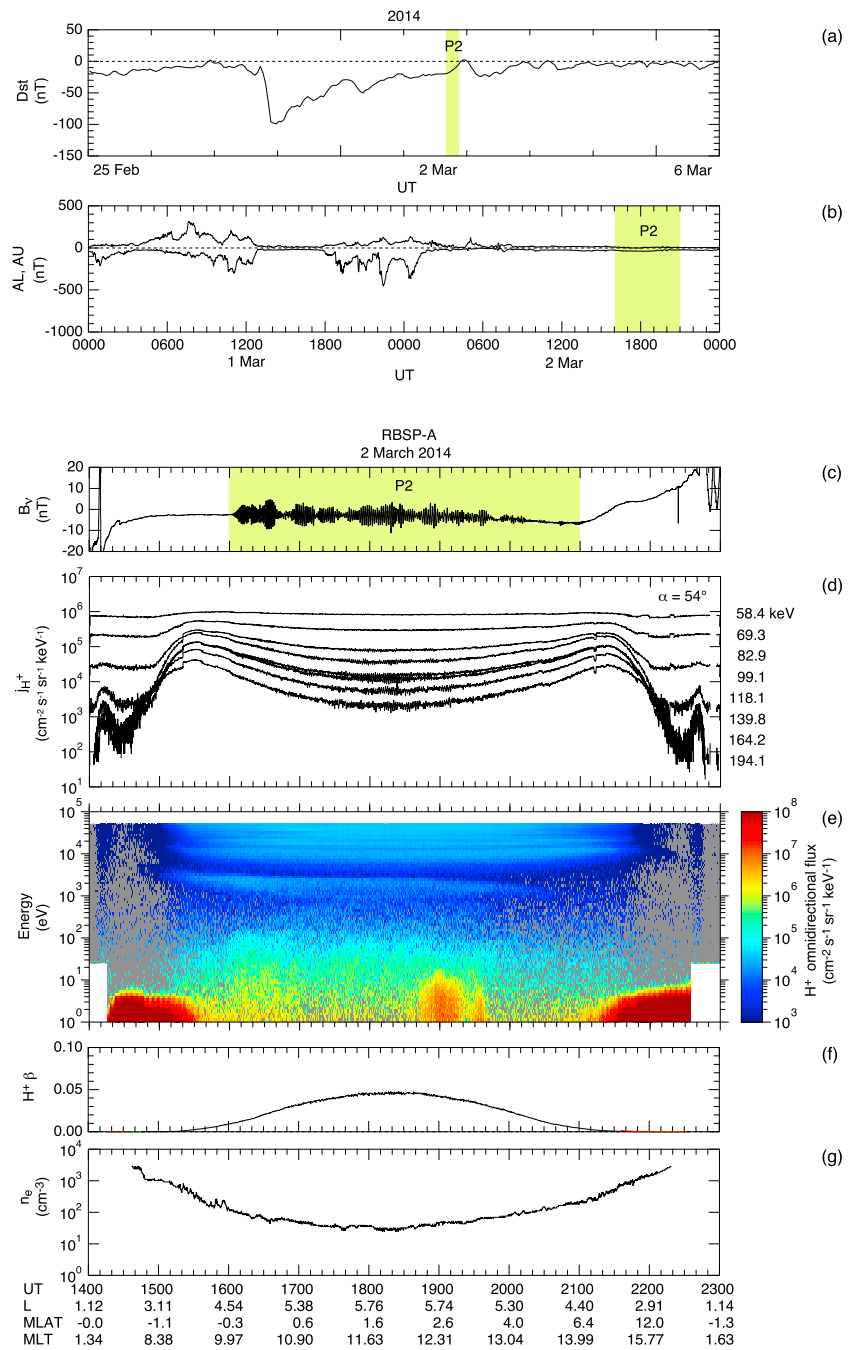


Figure 4. Geomagnetic indices and RBSP-A data covering the selected P2 wave event. (a) *Dst* index for 25 February to 6 March 2014. The shading indicates the time interval of P2 wave activity at RBSP. (b) Auroral electrojet indices covering the P2 wave event operation. (c) Radial component of the magnetic field. (d) Flux of ions detected by MagEIS at several selected energies and averaged in the α bin centered on 54° . (e) Omnidirectional flux of protons detected by HOPE. (f) Proton β calculated using HOPE data. (g) Electron number density determined using plasma wave spectra.

with *Dst* minimum reaching -99 nT on 27 February (Figure 4a). By the time the waves were observed, *Dst* had recovered to -20 nT. The *AE* index (Figure 4b) plotted for 2 days indicates that there was a moderate substorm activity prior to 0600 UT of 2 March. By the time the P2 waves were observed, the activity had nearly completely subsided.

Figures 4c–4g show perigee-to-perigee plots of selected RBSP-A data. The P2 wave activity is evident in the B_v time series (Figure 4c), which exhibits regular oscillations from 1600 UT to 2100 UT with considerable

amplitude modulation. The amplitude repeatedly exceeded 10 nT peak to peak. The flux of ions (assumed to be protons hence denoted J_{H^+}) measured by MagEIS and displayed at eight energy bins from 58 keV to 194 keV and averaged in the α bin centered on 54° (Figure 4d) also exhibits oscillations, which are coherent with the magnetic field oscillations as we will see below. Note that J_{H^+} data for the few energies below 100 keV are contaminated by noise, which is attributed to radiation damage to the detector. We include these data because wave-induced oscillations are sometimes detected despite the contamination. The J_{H^+} oscillations are strong around the spacecraft apogee (1825 UT). The energy spectrogram of the omnidirectional flux of H^+ ions measured by HOPE (Figure 4e) shows two populations, one below ~ 0.5 keV and the other above ~ 1 keV. The higher-energy population exhibits a stripe structure with multiple peaks located between ~ 1 keV and the instrument energy upper limit of 52 keV. The structure is similar to those reported by Ferradas et al. (2016) and referred to as multiple-nose structures. The proton β (Figure 4f), calculated using HOPE data, is <0.05 , justifying our low- β assumption for the plasmasphere. The electron number density (Figure 4g) varies smoothly with time (and L), reaching a minimum of $\sim 20 \text{ cm}^{-3}$ at the spacecraft apogee of $L = 5.8$. This leads us to conclude that the spacecraft was in the plasmasphere for the entire orbit, including the period of P2 waves (see also Figure 3c).

4.2. Dynamic Spectra

Figures 5a–5e are full-orbit dynamic spectra of the power spectral density (PSD) of the \mathbf{E} and \mathbf{B} fields observed by RBSP-A. In each PSD panel, the P2 waves produce a peak, labeled “P2”. The peak first appears at 1600 UT at 14 mHz, and as the spacecraft moves to the apogee (1825 UT), the frequency reaches a minimum of 9 mHz. On the inbound leg of the orbit, the frequency increases and reaches 17 mHz at 2100 UT. The steady peak at 24 mHz that appears in the E_v and E_ϕ spectra and labeled “N” (for noise) is an artifact (Takahashi, Denton, et al., 2015). The spectral power at the P2 peak is higher in the poloidal components (E_ϕ and B_v) than in the toroidal components (E_v and B_ϕ). However, the B_ϕ amplitude is as high as $\sim 50\%$ of the B_v amplitude, meaning significant poloidal-toroidal coupling. The compressional component (B_μ) is much weaker, but it still produces a clear peak in the dynamic spectra. A finite compressional component is an inevitable consequence of toroidal-poloidal mode coupling (e.g., Kiverson & Southwood, 1986) and also could be a result of finite plasma pressure (Chen & Hasegawa, 1991; Cheng & Qian, 1994). Note that P2 waves have a B_μ node at the magnetic equator, which is consistent with the low B_μ spectral power relative to B_v and B_ϕ .

We have additional evidence for the P2 wave mode. First, the P2 frequency is about twice the frequency of the fundamental toroidal (T1) wave, which is shown by a white or black line labeled “T1.” The T1 wave frequency was obtained by solving the toroidal wave equation for a dipole background magnetic field (Cummings et al., 1969). Here we specified the equatorial mass density using the electron density shown in Figure 4d and assumed that the average ion mass is 2 amu. In addition, we assumed the mass density to be constant along the magnetic field line (Takahashi, Denton, et al., 2015). Second, the E_ϕ - B_v cross phase (Figure 5f) is about 90° (orange pixels) in the P2 band. This cross phase value means that E_ϕ leads B_v by a quarter of the wave period, which is consistent with P2 waves observed slightly above the magnetic equator (MLAT > 0 , see Figure 3b) (e.g., Cummings et al., 1969). The P2 waves accompanied an E_ϕ perturbation even at MLAT = 0, which implies that the E_ϕ node was located slightly below the magnetic equator.

4.3. Azimuthal Wave Number: Two-Point Magnetic Field Measurements

Knowledge of the azimuthal wave number, m , is essential in discussing the generation mechanism of magnetospheric ULF waves. Evaluation of m is possible for the present P2 wave event using two methods: analysis of magnetic field phase delay between the two RBSP spacecraft and analysis of ion finite gyroradius (FGR) effects seen in energetic proton fluxes at each RBSP spacecraft.

We describe the magnetic field phase delay analysis first. Figure 6 is a 7 h dynamic display of spectral parameters computed from the B_v and B_μ components at the two RBSP spacecraft along with the relative distance of the spacecraft in the dipole coordinates. The positions of the two spacecraft are also printed at the bottom. An L conjunction occurred at 1841 UT, and during the period of P2 wave activity (1600–2100 UT), the L shell separation was <0.2 (Figure 6a), the MLAT separation was $<0.5^\circ$ (Figure 6b), and the MLT separation was <0.04 h ($\sim 0.6^\circ$ in longitude, Figure 6c). Figures 6d and 6e show the PSD of B_v at RBSP-A (denoted B_{vA}) and RBSP-B (denoted B_{vB}). Figure 6f shows the cross phase between B_{vA} and B_{vB} . Figures 6g–6i show the same parameters for the B_μ components.

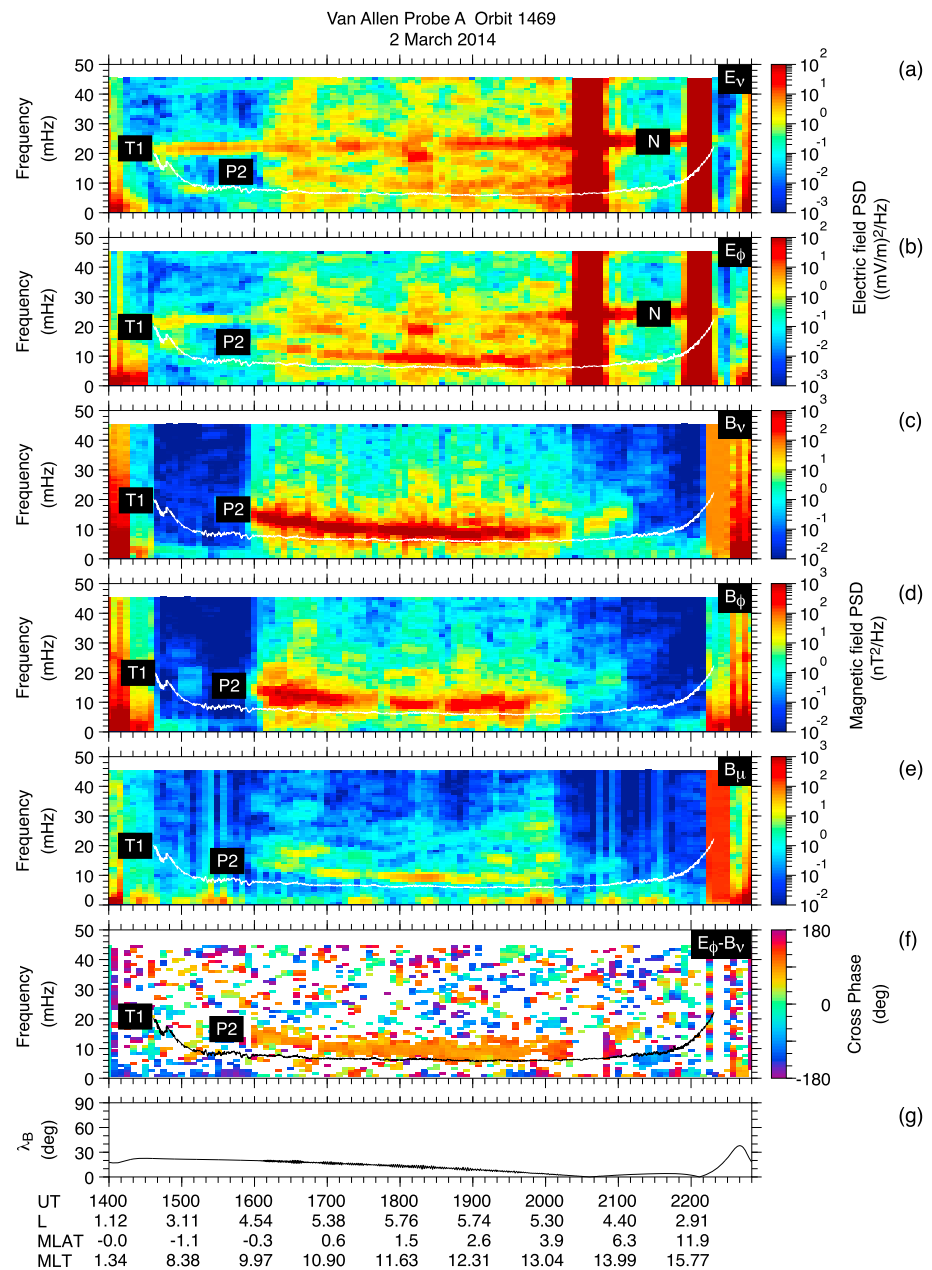


Figure 5. Full-orbit display of data from RBSP-A showing a continuous P2 wave activity on 2 March 2014. (a and b) PSD of the E_v and E_ϕ components in the MFA coordinates. The white line is the frequency of the fundamental toroidal mode (T1) wave calculated using a model described in the text. The spectral line labeled “N” is instrumental noise. (c–e) PSD of the three components of the magnetic field in the MFA coordinates. (f) Cross phase between E_ϕ and B_v displayed in color. The white pixels mean that coherence is lower than 0.7. (g) Angle of magnetic field elevation from the spacecraft spin plane. When this angle is small, error of the field components in the MFA coordinates becomes large, resulting in saturation of the \mathbf{E} field PSD as shown at ~ 2040 UT and ~ 2210 UT.

The dynamic spectra of the B_v and B_μ components are very similar between RBSP-A and RBSP-B, which is expected because the spacecraft were very close to each other. In the B_v cross phase spectra (Figure 6f), the P2 wave band appears in yellow to red colors, which means that RBSP-A leads RBSP-B by $\sim 90^\circ$ or RBSP-B leads RBSP-A by $\sim 270^\circ$ excluding the possibility of additional multiples of 360° . Note that the cross phase is displayed against the white background only when the coherence is > 0.7 . Outside of 1650–1940 UT, the $B_{vA}-B_{vB}$ cross phase is poorly defined in the P2 wave band, which can be attributed to larger L distances between the spacecraft.

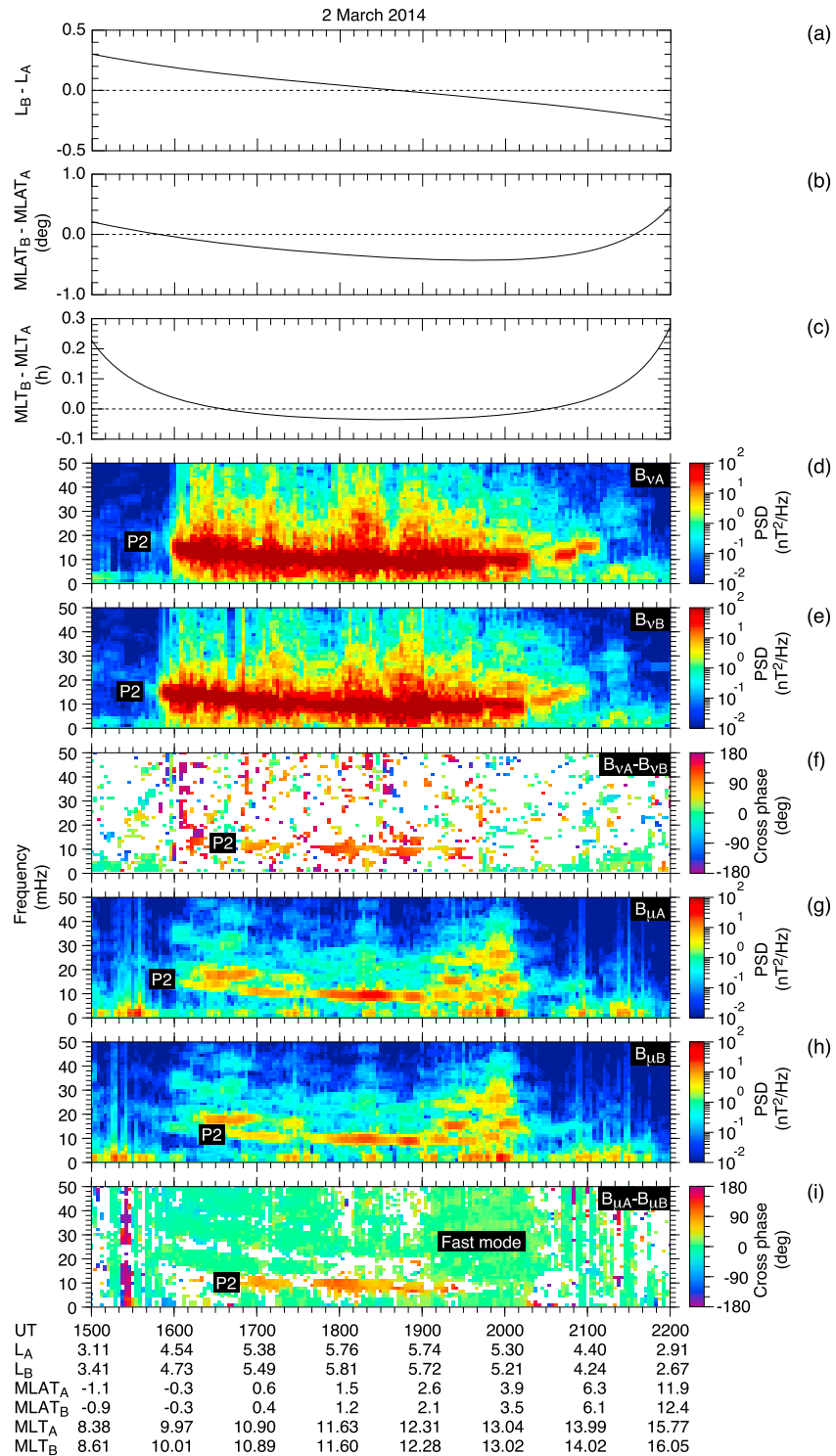


Figure 6. (a–c) Separation of the two RBSP spacecraft in the magnetic coordinates. (d) Dynamic display of the B_v PSD at RBSP-A. (e) B_v PSD at RBSP-A. (f) Cross phase computed from the B_v components at the two spacecraft. The cross phase is shown in color against the white background if the coherence is higher than 0.7. (g–i) Same as Figures 6d–6f, respectively, but for the B_μ components.

A very similar feature appears in the $B_{\mu A}$ - $B_{\mu B}$ cross phase spectra in the P2 wave band (Figure 6i). However, unlike the B_v components, the B_{μ} components are coherent at almost all frequencies and at all times. Moreover, the cross phase is nearly zero (light green) except in the P2 wave band. This broadband coherence occurs because fast mode waves of external origin reach the two spacecraft almost simultaneously as described by Takahashi, Denton, et al. (2015). In support of this scenario, the Time History of Events and Macroscale Interactions during Substorms D spacecraft, which was located near the magnetopause in the postnoon sector, detected broadband compressional oscillations very similar to those detected by RBSP. The spectral peaks appearing in the B_{μ} spectra above the P2 wave band could be a field line resonance effect that was reported by Takahashi, Waters, et al. (2015).

The interspacecraft phase delay can be examined in greater detail both in the time and frequency domains. Figure 7 illustrates a time domain technique. In this technique, we simply calculate the cross correlation (denoted γ) of magnetic field perturbations at the two spacecraft as a function of the time delay (denoted τ) and look for peaks in the γ versus τ plots. The calculation of γ was done in a 4 min moving data window. Figures 7a and 7b show the B_{vA} and B_{vB} time series and the corresponding γ function for a sample interval. The time series plots show nearly identical oscillations at the two spacecraft with a clear phase delay. The γ function exhibits a peak at $\tau = \tau_{\text{peak}}^- (< 0$, marked by a vertical dashed line) and another peak at $\tau = \tau_{\text{peak}}^+ (> 0$, marked by an arrowhead). A positive delay indicates propagation from RBSP-A to RBSP-B, which corresponds to westward propagation because RBSP-A was located to the east of RBSP-B. Conversely, a negative delay means eastward propagation. Figures 7c and 7d show the B_{μ} data in the same format. Assuming westward propagation, which will be justified below, we calculated the azimuthal wave number. Here we used the relationship $m = \Delta\theta/\Delta\phi$, where $\Delta\theta$ is the measured phase delay and $\Delta\phi$ is the longitudinal separation of the spacecraft. The phase delay is defined to be $\Delta\theta = 2\pi\tau_{\text{peak}}^+/T$, with the wave period T given by $T = \tau_{\text{peak}}^+ - \tau_{\text{peak}}^-$.

Figures 7e–7g show the results of the moving-window analysis for 1800–1900 UT. The γ value at $\tau = \tau_{\text{peak}}^+$ (denoted γ_{peak}^+ , Figure 7e) is generally higher for B_v than for B_{μ} (γ values lower than 0.5 are not shown). The wave frequency ($= T^{-1}$, Figure 7f) is very steady at ~ 10 mHz, consistent with the Fourier dynamic spectra shown in Figure 5. The m value is steady at ~ -200 at 1800–1815 UT for both B_v and B_{μ} . After 1815 UT, m for B_v varies considerably between -300 and -50 , and m for B_{μ} cannot be defined at many time steps because of low γ .

The cross-correlation analysis works best when there is only one outstanding sinusoidal wave. Fourier spectral analysis provides additional information on the phase delay when there are multiple oscillations. Figure 8 shows the results of Fourier cross spectral analysis of B_v and B_{μ} data for 1800–1815 UT, a time interval of nearly constant m according to Figure 7g. The spacecraft radial separation (ΔR_v) decreased from 270 km to 170 km, whereas the azimuthal separation (ΔR_{ϕ}) changed only slightly from -310 km to -330 km (RBSP-A was located east of RBSP-B) (Figure 8a). The separation in MLAT (not shown) changed also very slightly, from -0.49° to -0.51° . The time series plots of both B_v and B_{μ} (Figures 8b and 8c) indicate that oscillations at RBSP-A lead those at RBSP-B by approximately a quarter of the wave period. The cross phase spectra indicate that the phase delay is $\sim 100^\circ$ for both B_v (Figure 8f) and B_{μ} (Figure 8i) at the P2 frequency of 10 mHz. Because the average longitudinal separation of the spacecraft for the selected time interval was 0.50° , we get $m \sim -200$ assuming westward propagation. This result is in very good agreement with what we obtained in the cross-correlation analysis.

As stated above, the B_{μ} oscillations contain contributions from fast mode waves. The fast mode waves appear as higher-frequency perturbations on top of the 100 s oscillation associated with the P2 wave (Figure 8c) and produce a broad peak at ~ 25 mHz in the power spectra (Figure 8g). At this frequency, the coherence is high (Figure 8h) and the cross phase is close to zero (Figure 8i), indicating a phase velocity far greater than that of the P2 waves.

4.4. Azimuthal Wave Number: Ion FGR Effects

Remote sensing using ion FGR effects is a powerful technique in estimating the wavelength and propagation direction of waves with periods much longer than the local ion gyroperiod. The technique has been applied to Pc4–Pc5 waves observed by ATS-6 primarily in the dusk sector (Su et al., 1977), a compressional Pc5 wave observed by International Sun-Earth Explorer-1 in the dusk sector (Lin et al., 1988), compressional Pc5 waves observed by Active Magnetospheric Particle Tracer Explorers Charge Composition Explorer (AMPTE/CCE) in the dawn and dusk sectors (Takahashi, Cheng, et al., 1990), and a P2 wave observed by RBSP-A in the dusk-midnight sector (Min et al., 2017). These studies found the waves to be westward propagating with the

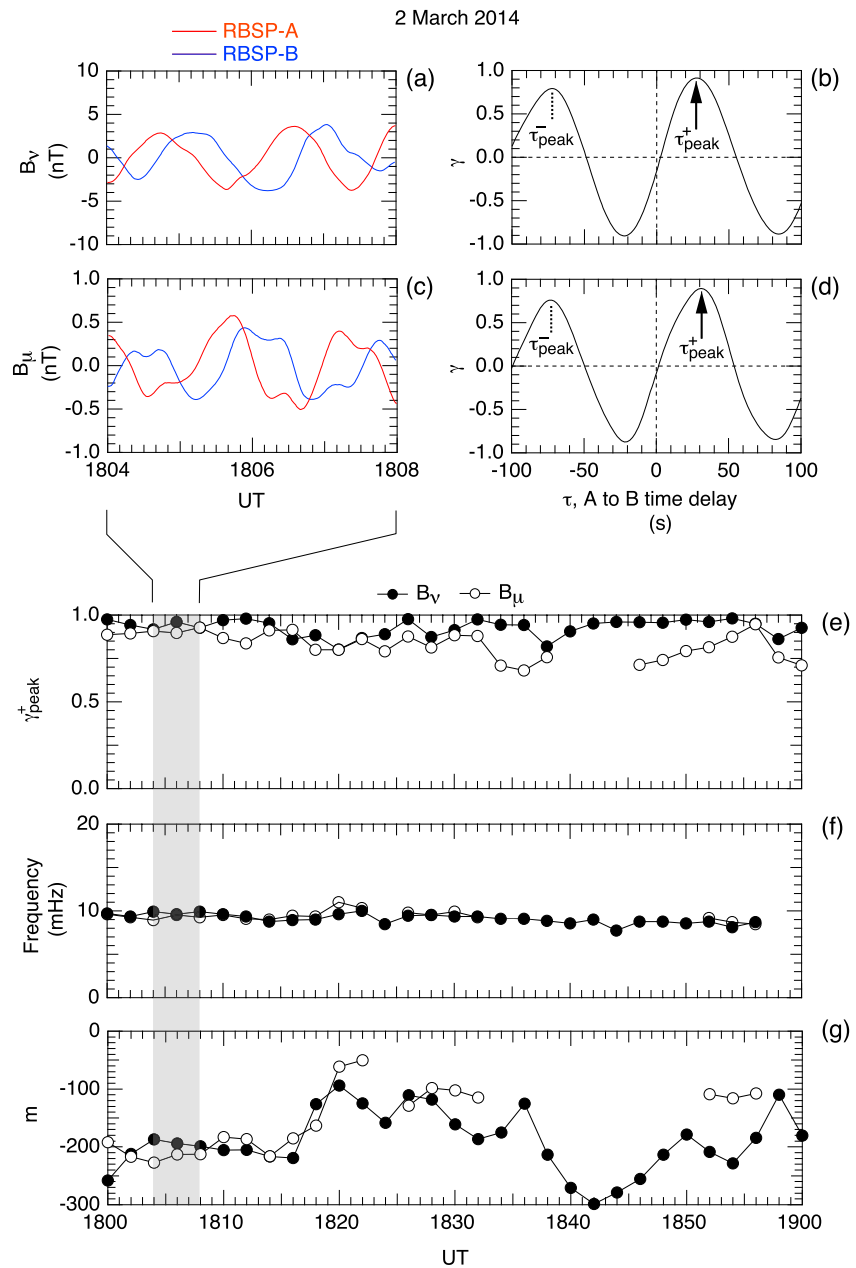


Figure 7. Cross-correlation analysis of RBSP magnetic field data. (a) B_v perturbations at RBSP-A and RBSP-B during a 4 min interval. (b) Correlation coefficient calculated from the data shown in Figure 7a and displayed as a function of time delay from RBSP-A to RBSP-B. The arrow indicates the peak in the positive τ domain corresponding to westward propagation. The vertical dotted line indicates the peak in the negative τ domain corresponding to eastward propagation. (c and d) Same as Figures 7a and 7b but for B_μ . (e) Peak value of the correlation coefficient in the positive τ domain, obtained by moving the 4 min data window in 2 min steps. (f) Frequency calculated from the time separation of the γ peaks. (g) Azimuthal wave number obtained using the time delay, wave frequency, and the spacecraft azimuthal separation as described in the text.

exception of the dawn-sector events at AMPTE/CCE. However, the AMPTE/CCE observation was explained by a strong eastward plasma convection that makes westward propagating waves in the plasma-rest frame appear eastward propagating in the spacecraft frame.

In the present study, the proton gyroperiod is of the order of 1 s, which is much shorter than the wave period ~ 100 s. The wave period is much longer than the spacecraft spin period (~ 11 s) also, which means that the wave fields are nearly static relative to the time for the detector to complete an azimuthal scan about the

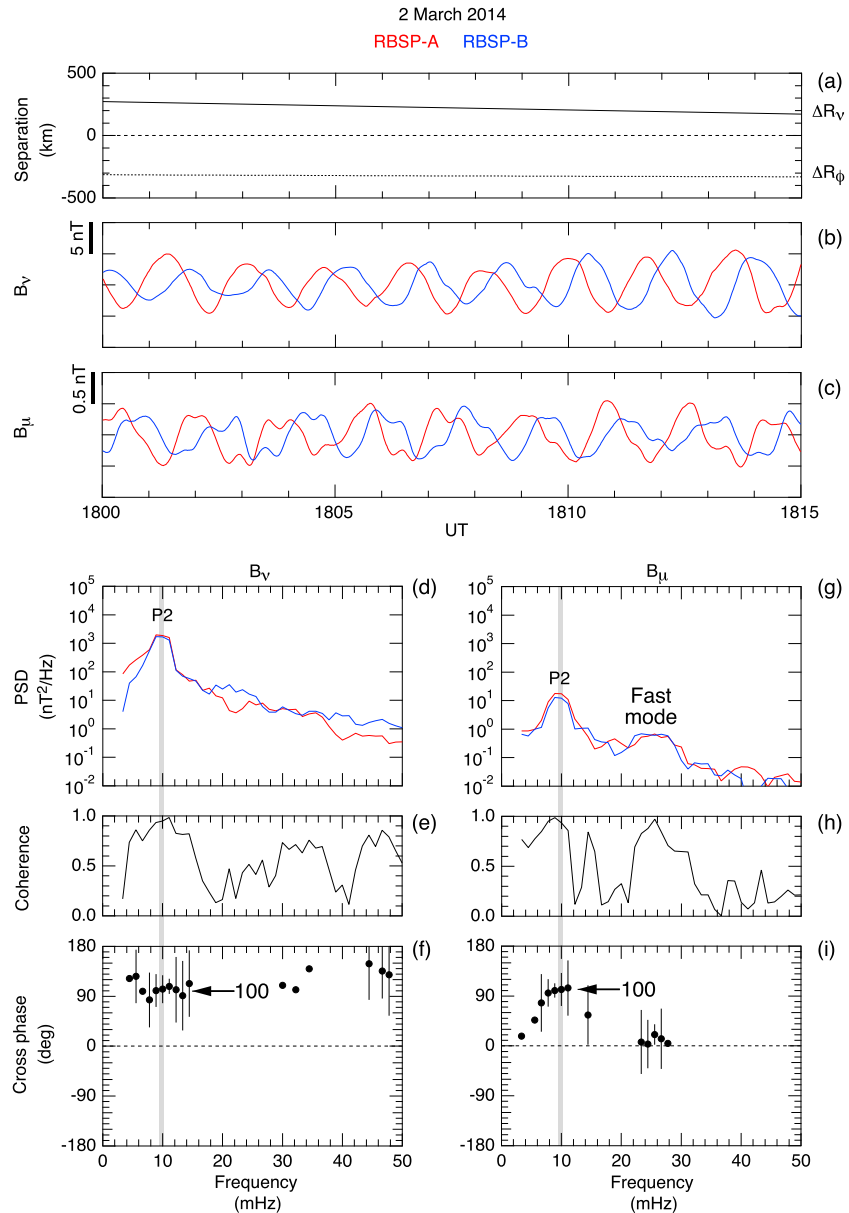


Figure 8. Relationship between magnetic field oscillations at RBSP-A and RBSP-B during 1800–1815 UT. (a) Distance of RBSP-B from RBSP-A in the radial (ΔR_v) and azimuthal (ΔR_ϕ) directions. (b) Perturbations in B_v . (c) Perturbations in B_μ . (d–f) Power spectra, coherence and cross phase computed from the B_v time series. Three-point averaging of the spectral matrices in the frequency domain is done to obtain the spectral parameters. The vertical bars in the cross phase panel indicate the 95% confidence limits as described by Green (1976). (g–i) Same as Figures 8d–8f, respectively, but for the B_μ components.

background magnetic field. The location of the guiding centers of particles detected by a spacecraft depends on the particle energy and the look direction of the particle detector (Kivelson & Southwood, 1983; Lin et al., 1988; Min et al., 2017). This means that oscillations of particle fluxes are affected by \mathbf{E} and \mathbf{B} field perturbations at the guiding centers. This effect allows us to estimate the wavelength of waves causing the flux oscillations from the phase delay between particle flux oscillations measured at multiple energies and/or look directions. For a wave propagating azimuthally with an azimuthal wavelength of λ_ϕ and a frequency of ω , the perturbation of particle fluxes δj observed at a spacecraft can be expressed as

$$\delta j \propto \exp[i(2\pi \frac{\vec{\rho}_G \cdot \mathbf{e}_k}{\lambda_\phi} - \omega t)], \quad (8)$$

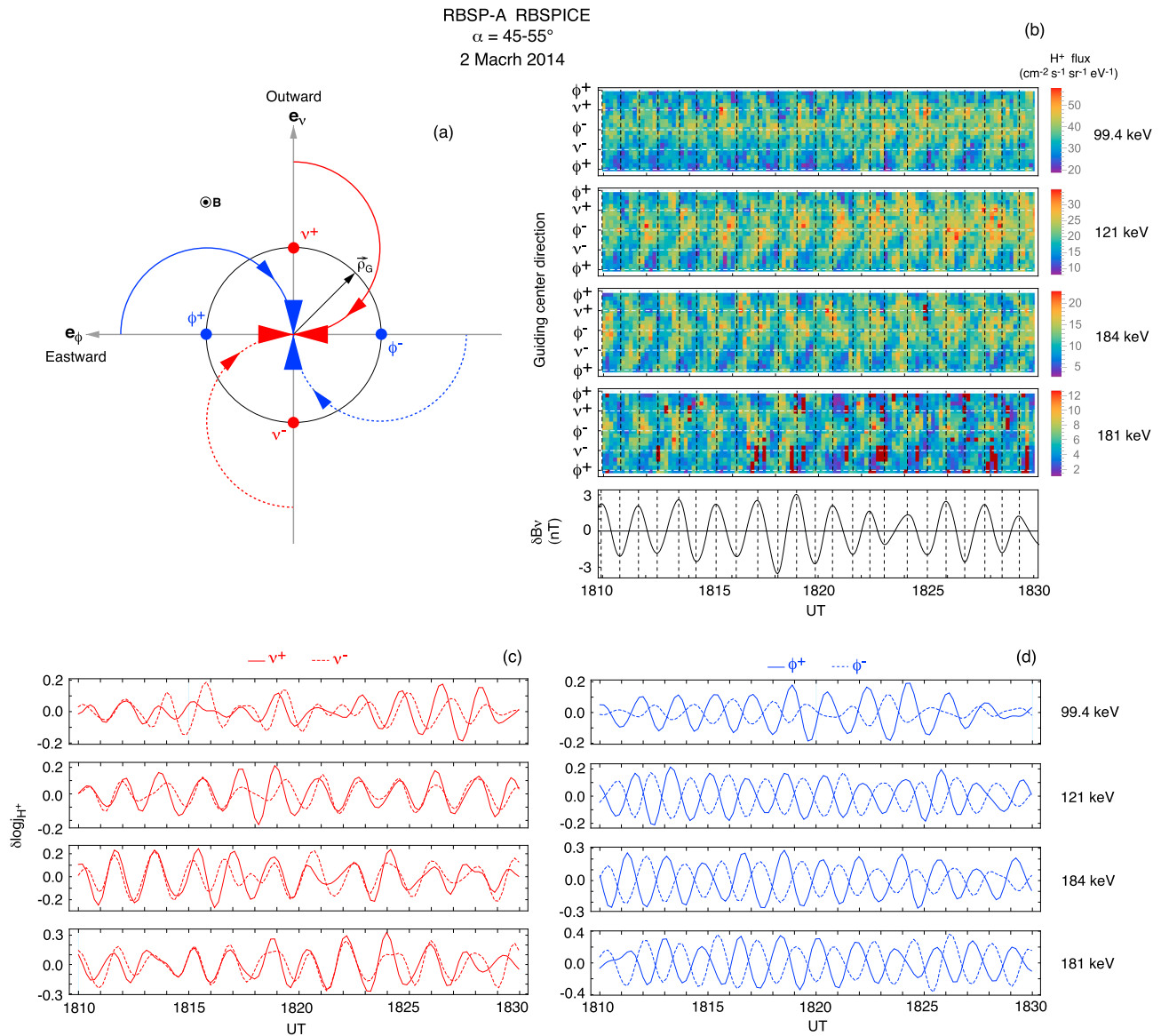


Figure 9. FGR effects shown in proton fluxes measured by RBSPICE on RBSP-A. (a) Geometry of proton measurements by RBSPICE. Four representative detector look directions and the corresponding guiding center locations are illustrated. (b) Color-coded proton flux perturbations in the 45–55° pitch angle bin at four energies, displayed as a function of time and the guiding center direction with respect to the spacecraft, projected to the v - ϕ plane of the MFA coordinates. (b) Filtered B_v . Vertical dashed lines are drawn through the peaks. (c) Perturbations of fluxes measured at telescope look directions corresponding to guiding centers located on the positive (v^+) and negative (v^-) v meridian planes. (d) Perturbations of fluxes measured at telescope look directions corresponding to guiding centers located on the positive (ϕ^+) and negative (ϕ^-) ϕ meridian planes.

where $\vec{\rho}_G$ is the guiding center position defined in the plane perpendicular to the ambient magnetic field and \mathbf{e}_k is the direction of wave propagation. By substituting $\lambda_\phi = 2\pi R_c/m$, where R_c is the distance from the dipole axis (see Figure 3b), we obtain an alternative expression

$$\delta j \propto \exp\left[i\left(m\frac{\vec{\rho}_G \cdot \mathbf{e}_k}{R_c} - \omega t\right)\right]. \quad (9)$$

We have applied the FGR remote sensing technique developed for RBSPICE data by Min et al. (2017) to our P2 waves. Figure 9 illustrates the analysis for 1810–1830 UT, during which RBSPICE detected clear j_{H^+} oscillations in several energy bins. Figure 9a illustrates the relationship between the detector look direction and the location of the proton guiding center. Four representative guiding center locations are shown by large colored dots placed on the positive and negative v and ϕ axes. They are labeled v^+ , v^- , ϕ^+ , and ϕ^- , respectively.

Table 1
FGR Remote Sensing Results

W (keV)	α (deg)	ρ_{\perp} (km)	γ	τ (s)	λ_{ϕ} (km)	V_{ϕ} (km/s)	m
121	50	250	0.91	23.6	1,080	10.6	-215
121	130	250	0.82	23.9	1,070	10.5	-218
148	50	276	0.90	24.0	1,170	11.5	-198
181	50	305	0.85	26.3	1,180	11.6	-196
181	130	305	0.81	26.4	1,180	11.6	-197

This figure shows a simple case of the detector look direction being perpendicular to the magnetic field. In the real observation with a variable magnetic field direction, a situation equivalent to the illustrated case can be achieved by sorting the fluxes from the multiple telescopes into α and guiding center direction bins.

The top four panels of Figure 9b show the proton fluxes measured by RBSPICE in the 44–55° α bin, displayed as a function of time and guiding center direction for four energies. Each pixel has a size of one spin period (~ 11 s) along the time axis, and the time tag for the pixel is the center of the spin. Each panel shows a regular variation of the flux intensity, which is synchronized with the magnetic field perturbation shown in the bottom panel of Figure 9b. The timing of the flux peak depends on the guiding center location. For example, in the 181 keV panel of Figure 9b, the peak first appears at ϕ^+ ($\vec{\rho}_G$ directed east of the spacecraft) and then moves to ϕ^- ($\vec{\rho}_G$ directed west of the spacecraft), passing v^+ and v^- ($\vec{\rho}_G$ longitudinally aligned with the spacecraft) in between. A qualitatively same pattern is seen at the three other energies, but the amount of time delay between the ϕ^+ and ϕ^- directions decreases as energy becomes lower and the corresponding gyroradius becomes smaller. This means almost purely azimuthal westward propagation of the wave phase fronts. A more detailed explanation of this effect is shown in Figure 10 of Min et al. (2017).

The azimuthal propagation is more clearly shown in Figures 9c and 9d. In Figure 9c, we compare the flux oscillations for v^+ and v^- that have been band-pass filtered between ~ 5 mHz and ~ 15 mHz. There is little phase delay between the two directions, which means that the wave does not propagate radially. In contrast, Figure 9d shows that there is an $\sim 180^\circ$ phase difference between the ϕ^+ and ϕ^- directions, implying that the wave propagates azimuthally with a wavelength about 4 times the gyroradii of the protons considered here.

To determine the m value, we calculated the cross correlation and cross phase between j_{H^+} oscillations at the v^+ and ϕ^- guiding center directions. The results are summarized in Table 1 for $\alpha = 50^\circ$ and its conjugate $130^\circ (= 180^\circ - \alpha)$. Particles with conjugate pitch angles cross the magnetic equator in opposite directions along the magnetic field with their velocity vectors making the same angle to the equatorial plane. We used data for 121–181 keV, and the results are shown when $\gamma > 0.6$. The five estimates listed in the table indicate m to be in a narrow range of -197 to -215 . The corresponding ranges of λ_{ϕ} and V_{ϕ} are 1,070–1,180 km and 10.5–11.6 km/s, respectively.

The FGR analysis results differ somewhat from the magnetic field cross-correlation results shown in Figure 7. In the time interval 1810–1830 UT chosen for the FGR analysis, the m number from the B_y analysis varied between -219 and -94 , with an average of -156 (Figure 7g). Therefore, the FGR analysis overestimates $|m|$ by $\sim 20\%$. We consider the results from the two techniques to be in reasonable agreement.

4.5. Doppler Shift

The observed P2 waves had a large m number, and correspondingly a small azimuthal phase velocity, which means that the observed frequency was possibly Doppler shifted. For the $m = -200$ that is determined in section 4.2, the azimuthal wavelength (λ_{ϕ}) at the spacecraft is 1,160 km. The spacecraft was moving westward at a velocity ($V_{\phi SC}$) of 0.9 km/s relative to the plasmaspheric plasma, which is assumed to be corotating with the Earth. The frequencies in the corotating system (f_{CR}) and at the spacecraft (f_{SC}) are related as

$$f_{SC} = f_{CR} - |V_{\phi SC} / \lambda_{\phi}|. \quad (10)$$

By substituting the values of λ_{ϕ} and $V_{\phi SC}$ into equation (10), we find the frequency 10.1 mHz observed in the spacecraft frame of reference is upshifted by 0.8 mHz to 10.9 mHz in the corotating frame of reference. We conclude that the Doppler shift is small.

5. Proton Drift-Bounce Resonance

This section describes energy and pitch angle dependence of the phase of ion flux oscillations observed by RBSP and interpretation of the data in terms of theory of drift-bounce resonance.

5.1. Brief Review of the Theory

The resonance described by equations (1)–(3) leads to energy (and a lesser degree pitch angle) dependence of the amplitude and phase of j_{H^+} oscillations. To see this, let us assume that energy modulation of individual particles (denoted δW) causes a time-dependent shift of the proton energy spectrum and that this shift gives rise to the modulation of j_{H^+} (denoted δj_{H^+}) detected by an instrument with fixed energy windows. According to Takahashi, McEntire, et al. (1990) and Chen and Hasegawa (1994), δj_{H^+} and the magnetic field radial component (denoted δB_v) of a P2 wave, when observed at the magnetic equator, are related as

$$\delta j_{H^+} \propto \pm \delta W \alpha \frac{\pm i \cos \theta_b}{(\omega - m\omega_d)^2 - \omega_b^2} \delta B_v, \quad (11)$$

where θ_b is the bounce phase defined in terms of particle velocity parallel to the magnetic field (v_{\parallel}) and distance along the field line (s) as $\theta_b = \int_{eq}^s ds \omega_b / v_{\parallel}$ (e.g., Southwood & Kivelson, 1981). We consider only the $N = \pm 1$ resonance and ignore the FGR effect. At the equator, θ_b is 0 or 180° depending on whether a particle is moving northward or southward, and the corresponding value of $\cos \theta_b$ is 1 or -1 . By including a small imaginary part in the wave frequency ω (Southwood & Kivelson, 1981), one finds that at the resonance, $\text{Re}(\omega) - m\omega_d = \pm \omega_b$, the denominator of equation (11) becomes essentially pure imaginary, leading to a δj_{H^+} - δB_v cross phase of 0 or 180°. At energies away from the resonance, the cross phase approaches $\pm 90^\circ$. Evaluation of the factors (e.g., the energy dependence of the particle phase space density) that are not included in the abbreviated expression on the right-hand side of equation (11) indicates that the phase of δj_{H^+} relative to δB_v advances with energy across the high-energy resonance when the proton phase space density decreases with energy (Takahashi, McEntire, et al., 1990) as commonly observed in the ring current at energies above 100 keV.

The δj_{H^+} - δB_v cross phase at the resonance can be understood by examining the guiding center orbits of resonant particles that are illustrated in Figures 1a and 1b. The yellow squares in these figures indicate the location of an equatorial spacecraft. The illustrated orbits pass the δE_ϕ maxima multiple times and pass the spacecraft at a longitude where $\delta E_\phi = 0$ at all magnetic latitudes along the magnetic field line. The largest acceleration of the particles occurs when they pass the δE_ϕ maxima, which are longitudinally separated from the spacecraft by $(n + \frac{1}{4})\lambda_\phi$, where n is an integer. This means that the particle energy modulation carries the information of δE_ϕ that is $(n + \frac{1}{4})\lambda_\phi$ away from the spacecraft, which translates to a δj_{H^+} - δE_ϕ cross phase of $\pm 90^\circ$ at the spacecraft. Because there is a phase difference of $\pm 90^\circ$ between δE_ϕ and δB_v of poloidal standing waves, the δj_{H^+} - δB_v cross phase is 0 or 180° at the spacecraft position. Note that because δE_ϕ of a P2 wave has a node at the magnetic equator, it is necessary to use δB_v as a reference signal in calculating the phase of δj_{H^+} when observations are made at or very near the magnetic equator. Use of δB_v is also preferred because not all spacecraft carry an electric field experiment.

We emphasize that the description presented above applies only to observations made at the equator. In observations away from the equator, θ_b is no longer equal to 0 or 180°, and a term involving $\sin \theta_b$ appears on the r.h.s. of equation (11) (e.g., Southwood & Kivelson, 1981). As a simple example, let us still assume a P2 wave but consider particles mirroring (local pitch angle = 90°) at the location of a spacecraft that is located off the equator. For these particles, the cross phase between δE_ϕ and δW is zero, leading to 0 or 180° (instead of $\pm 90^\circ$) cross phase between δj_{H^+} and δE_ϕ at the spacecraft. This situation is quite similar to equatorial observations of particle flux oscillations associated with a P1 wave (Dai et al., 2013).

5.2. Analysis of MagEIS Data

We examine whether the expected signatures of the drift-bounce resonance appear in proton data from MagEIS. MagEIS measures j_{H^+} using a single telescope in 20 energy bins covering from <100 keV to >1 MeV. The pitch angle distribution is obtained by accumulating counts in sectors defined in the spacecraft spin phase Φ_{spin} . This measurement geometry was illustrated in Figure 2.

During the P2 wave event, MagEIS measurements were made in evenly spaced 32 Φ_{spin} sectors, each covering 11.25° (there were 27 sectors prior to 10 October 2013). The sectors are labeled by the sector number that starts from 0 and ends at 31. Sector 0 covers the Φ_{spin} range of 0–11.25°. The pitch angle for a sector is defined

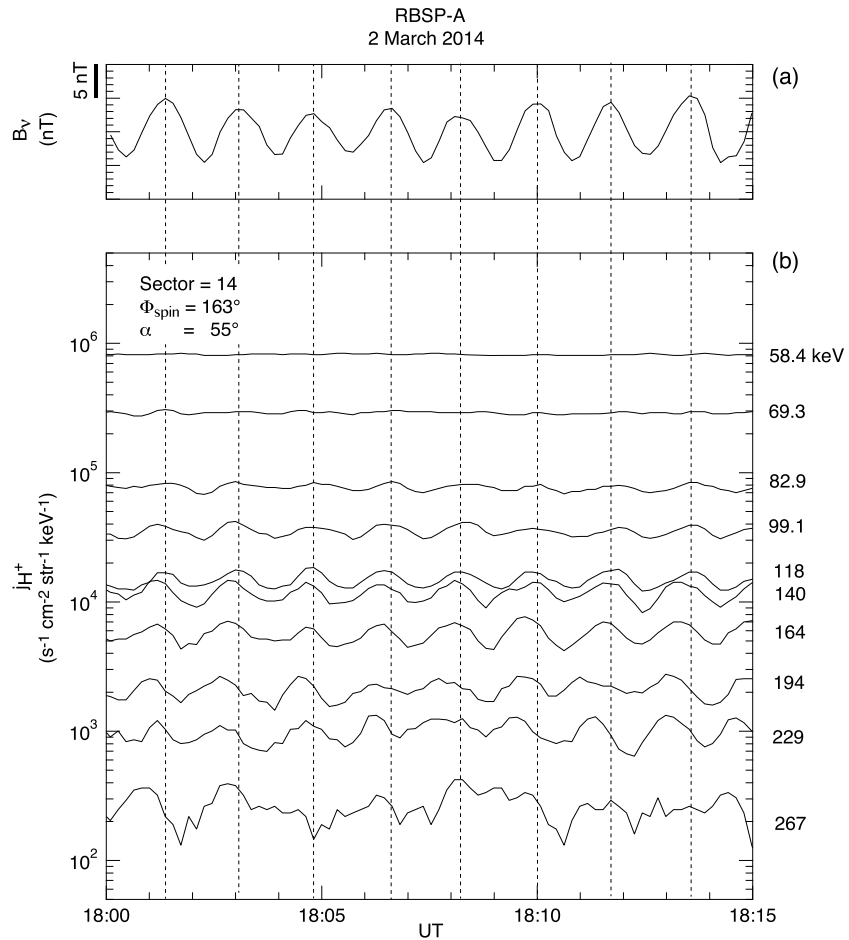


Figure 10. Data from RBSP-A for a 15 min period during the P2 wave event. (a) Magnetic field B_v component. Vertical dashed lines are drawn through the peaks. (b) Proton fluxes measured by the MagEIS proton telescope in sector 14, which corresponds to $\Phi_{spin} = 163^\circ$ and $\alpha = 55^\circ$.

by referring to the magnetic field measured when Φ_{spin} is at the center of the sector. Because the detector look direction sweeps a cone, instead of a plane, we need to pay attention to the look direction in addressing FGR effects in the measured j_{H^+} .

Figure 10 shows oscillations in B_v and j_{H^+} at 10 energies, observed by RBSP-A at 1800–1815 UT. The j_{H^+} data are taken from sector 14, which corresponds to $\Phi_{spin} = 163^\circ$ and $\alpha = 55^\circ$. Three-point smoothing has been applied to the j_{H^+} time series. The j_{H^+} oscillations are synchronized with the B_v oscillation. Oscillations at 58.4 keV and 69.3 keV are very weak due to noise attributed to detector radiation damage, but we can still see some regular oscillations at these energies when there is a strong B_v perturbation. The oscillations at 229 keV and 267 keV are irregular as a result of poor counting statistics. At energies higher than 267 keV, the particle counts were too low for determining the presence of oscillations associated with the P2 wave.

Energy dependence is evident in the phase delay between B_v and j_{H^+} . By following the vertical dashed lines, we find that j_{H^+} oscillates in phase with B_v at 82.9 keV and 99.1 keV. As the energy increases, the j_{H^+} peaks occur increasingly earlier than the B_v peaks. At 194 keV, j_{H^+} leads B_v by approximately a quarter of the wave period, which is equivalent to a phase difference of 90° . Qualitatively the same observations have been reported in previous studies (Kokubun et al., 1989; Korotova et al., 2015; Su et al., 1977, 1979; Takahashi, McEntire, et al., 1990).

The j_{H^+} oscillations depend on the pitch angle as well. Figure 11 shows the spin phase dependence of j_{H^+} measured at 139.8 keV in the same 15 min interval that was shown in Figure 10. Figure 11a is a schematic of the spacecraft location relative to the Sun and the Earth, the direction of the spacecraft spin axis, and the orbits of ions with the same energy but detected at spin phases 180° apart. Both spin phases correspond to $\alpha = 90^\circ$.

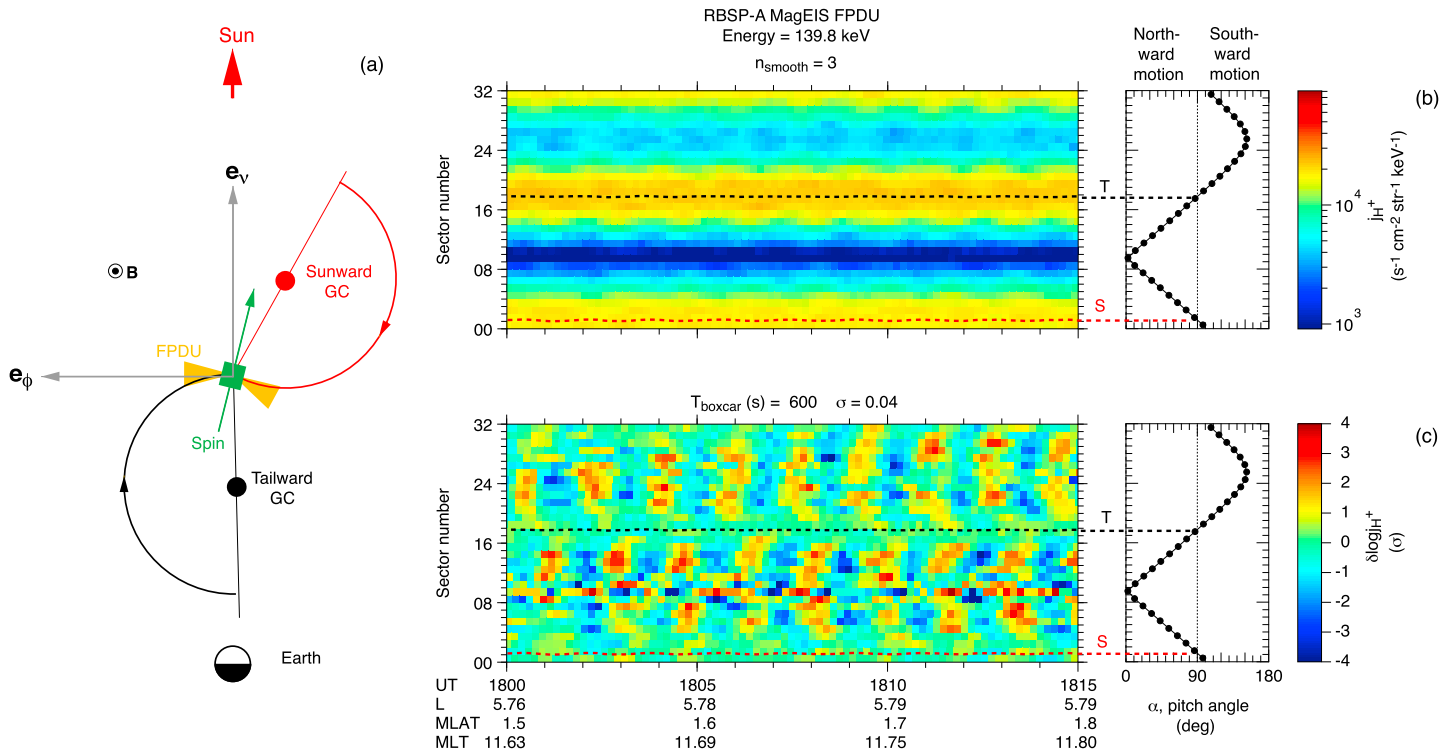


Figure 11. (a) Geometry of proton flux measurements by MagEIS. See text for explanation. (b) Proton flux at 139.8 keV displayed as a function of UT and sector number. The flux is smoothed by a three-point running average over time. The color bar is automatically adjusted to cover 2 orders of magnitude with the center value matching the median of all sectorized samples shown. The relationship between the sector number and the pitch angle is shown on the right. The horizontal dashed lines indicate 90° pitch angle, which occurs twice with the guiding center located sunward (red) and tailward (black) of the spacecraft. (c) Perturbation of the logarithm of the flux, $\delta \log j_{H^+}$, about its 600 s running mean, shown in the same format as Figure 11b. The color key is scaled to the standard deviation (σ) of $\delta \log j_{H^+}$.

For simplicity, the spacecraft is placed at noon and at the magnetic equator, and only one ion energy is considered. Instances of $\alpha = 90^\circ$ occur twice per spin. At one instance, the guiding center (GC) is located sunward of the spacecraft, as shown in red. At the other instance, the GC is located tailward of the spacecraft, as shown in black. Because the detector look direction is not perpendicular to the spacecraft spin axis, the two guiding centers and the spacecraft spin axis are not aligned. Figure 11b shows the raw j_{H^+} values (except for the three-point smoothing over time), while Figure 11c shows the perturbation of $\log j_{H^+}$ about its 600 s running mean. Because the baseline flux level had an Earthward gradient (see Figure 4d), fluxes shown in Figure 11b are higher in sectors that cover the tailward guiding centers (marked by the black horizontal dashed line) than in sectors that cover the sunward guiding centers (red dashed line). Also, because the telescope look direction sweeps over a cone, the pitch angle coverage is asymmetric about 90°, leading to a gap at 150–180° in this example.

In Figure 11c, it is clear that (a) oscillations are weak at $\alpha = 90^\circ$, (b) peaks alternate between low ($<90^\circ$) and high ($>90^\circ$) α domains, and (c) fluxes nearly parallel ($\alpha \sim 0^\circ$) or antiparallel ($\alpha \sim 180^\circ$) to the magnetic field lead those measured perpendicular to the magnetic field ($\alpha \sim 90^\circ$). These features are qualitatively the same as those reported for a P2 wave detected by the AMPTE/CCE spacecraft (Takahashi, McEntire, et al., 1990). The alternating peaks about $\alpha = 90^\circ$ can be explained by particle motion in an antisymmetric electric field structure (see Figure 1). Because the satellite was within 2° of the magnetic equator, α at the spacecraft is practically equal to α_{eq} .

Figures 12a and 12b summarize the pitch angle dependence of j_{H^+} oscillations at 139.8 keV. Guiding center directions are distinguished by using different symbols: open red circles for sunward guiding centers and filled black circles for tailward guiding centers. The PSD of $\delta \log j_{H^+}$ (Figure 12a) is peaked at $\alpha \sim 45^\circ$ and its conjugate $\alpha \sim 135^\circ$ and exhibits a minimum at $\alpha \sim 90^\circ$. The $\delta B_v - \delta \log j_{H^+}$ cross phase (Figure 12b) exhibits a large difference between protons moving northward ($\alpha < 90^\circ$) and southward ($\alpha > 90^\circ$). The cross phase for the sunward guiding centers is lower than that for tailward guiding centers. We attribute this difference to

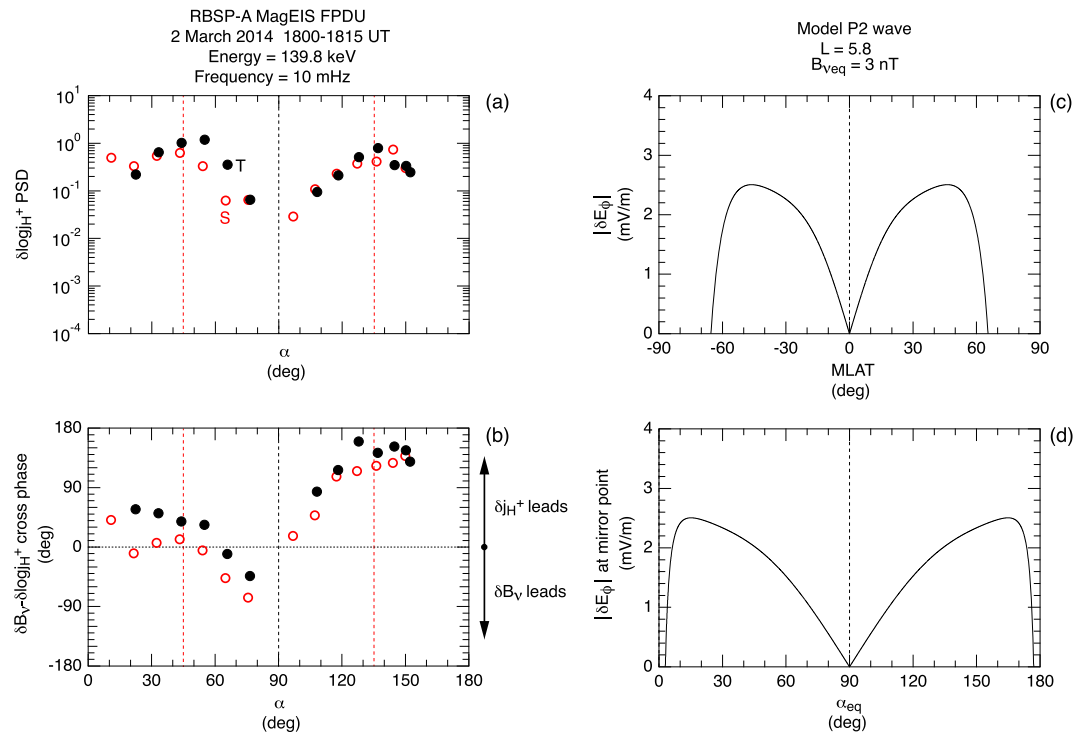


Figure 12. Spectral parameters of proton flux oscillations observed by RBSP-A at 139.8 keV plotted as a function of the pitch angle at the spacecraft. The parameters are evaluated at the frequency, 9.2 mHz, of the B_v oscillation. (a) PSD of $\delta \log j_{H^+}$. Vertical lines are drawn at 50° and 130° to mark the PSD peaks. Sunward (S, red open circles) and tailward (T, black solid circles) guiding centers are distinguished. (b) Cross phase between B_v and $\delta \log j_{H^+}$. (c) Electric field amplitude of a P2 wave, obtained using the poloidal wave equation of Cummings et al. (1969) and plotted as a function of magnetic latitude along a field line at $L = 5.8$. (d) The amplitude of the model wave electric field at the mirror point of a particle having the equatorial pitch angle specified on the horizontal axis.

the finite azimuthal distances between the particle detector and the guiding centers as we describe next. Overall, the results shown in Figures 12a and 12b are very similar to those reported in an AMPTE/CCE study of a dayside P2 wave event (Takahashi, McEntire, et al., 1990).

The pitch angle dependence of the amplitude of the j_{H^+} oscillations can be explained by the electric field mode structure of a P2 wave illustrated in Figure 12c. The structure was obtained by solving the poloidal mode equation of Cummings et al. (1969) with a field line mass density variation specified as $\rho = \rho_{eq}(R/LR_E)^{-1}$, where the equatorial mass density ρ_{eq} is set to 60 amu/cm^3 to match the theoretical eigenmode frequency with the observed P2 wave frequency. The value of the plotted δE_ϕ corresponds to the equatorial δB_v of 3 nT, which is comparable to the observed values. δE_ϕ reaches the maximum (antinode) of 2.5 mV/m at $\text{MLAT} = \pm 46^\circ$. Figure 12d shows the relationship between α_{eq} of a particle (horizontal axis) and the magnitude of δE_ϕ (vertical axis) that the particle sees at the northern and southern mirror points, obtained assuming a dipole magnetic field. The values of α_{eq} corresponding to the mirror latitudes of $\pm 46^\circ$ are 15° and its conjugate 165° . This means that the electric field amplitude that a particle sees monotonically increases as a function of $|\alpha_{eq} - 90^\circ|$ in the α_{eq} range of $15 - 165^\circ$. In the observation, $\delta \log j_{H^+}$ peaks at $\alpha \sim 45^\circ$ and 135° instead of 15° and 165° . This can be due to the low particle fluxes at small pitch angles (see Figure 11b).

Figure 13 summarizes the energy dependence of the phase of j_{H^+} oscillations at RBSP-A observed at 1800–1815 UT. We selected Φ_{spin} sectors corresponding to $\alpha = 55^\circ$ (northward moving particles) and $\alpha = 128^\circ$ (southward moving particles), which are nearly conjugate. Figure 13a shows the projection of the guiding center locations to the μ - ϕ plane of the MFA coordinates for the lower 10 energies of the MagEIS proton detector.

Figure 13b shows the $\delta B_v - \delta \log j_{H^+}$ cross phase calculated at the observed wave frequency of 10.1 mHz and displayed if the $\delta B_v - \delta \log j_{H^+}$ coherence at this frequency exceeds 0.6. In each sector, the cross phase increases with

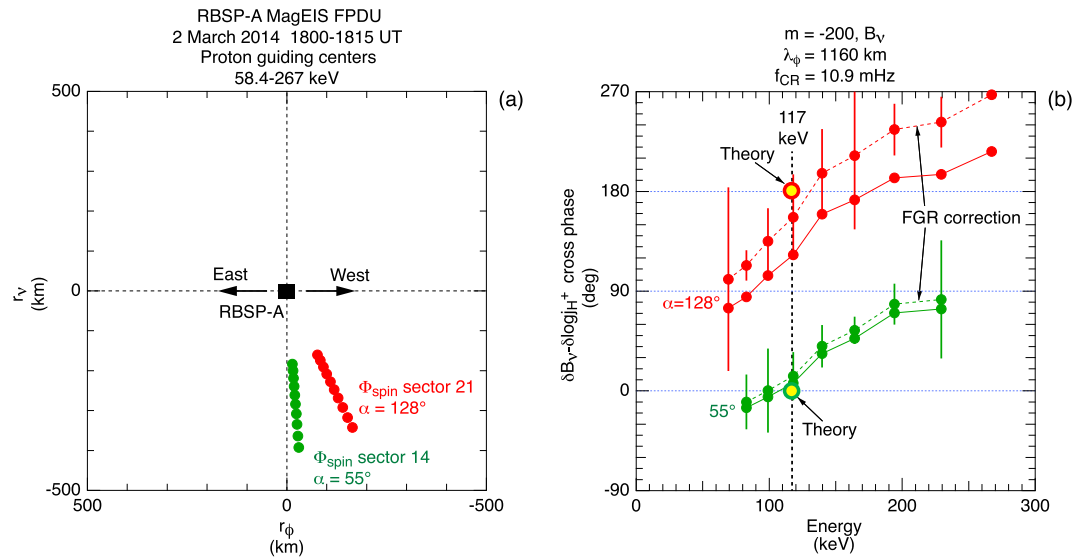


Figure 13. Energy and pitch angle dependence of the phase of j_{H+} oscillations observed by RBSP-A MagEIS at 1800–1815 UT. (a) Guiding center locations in the v - ϕ plane of the MFA coordinates. The color of the data points indicates the sector number and the corresponding pitch angle at the satellite. (b) Cross phase between oscillations in B_V and $\log j_{H+}$, plotted as a function of energy for the two selected sectors. The data points connected by a dashed line indicate values after an FGR correction has been made assuming $m = -200$. Error bars are added to these data points. The vertical dashed line indicates the energy of $\alpha = 55^\circ$ and $\alpha = 128^\circ$ protons that are in drift-bounce resonance with a P2 wave having $m = -200$ and $f_{CR} = 10.9$ mHz. Theory predicts the $\delta B_V - \delta \log j_{H+}$ cross phase to be 0 or 180° at this energy.

energy. However, there is a significant separation between the sectors, which is attributed to the difference in particle bounce phase.

We have corrected the cross phase by taking into account the FGR effects, and the results are shown in Figure 13b by data points connected by dashed lines. The correction was done by subtracting the phase $2\pi \vec{\rho}_G \cdot \mathbf{e}_k / \lambda_\phi$ (see equation (8)) from the raw cross phase shown in Figure 13b, where \mathbf{e}_k is assumed to be directed in the $-\mathbf{e}_\phi$ direction. To specify λ_ϕ , we adopted $m = -200$ that is determined from the B_V cross-correlation analysis described in section 4.3. This correction moves the cross phase data points upward, for $\alpha = 128^\circ$ in particular. We have added error bars to the corrected cross phase data points following Bendat and Piersol (1971).

We then solved equation (1) using the Hamlin et al. (1961) formula for ω_a and ω_b to find the energy of protons that are in high-energy ($N = -1$) resonance with the P2 wave for the selected α values. We assumed $m = -200$ and the wave frequency in the corotating frame of reference (f_{CR}) to be 10.9 mHz. The vertical dashed line indicates the resonance energy, 117 keV, averaged between the solutions for $\alpha = 55^\circ$ and $\alpha = 128^\circ$. The solutions differ only by 1.1 keV between these α values.

There are a few important features to be noted in Figure 13b:

1. The cross phase is an increasing function of energy at both pitch angles. The corrected phase increases from -10° (83 keV) to 83° (229 keV) at $\alpha = 55^\circ$, and from 101° (69 keV) to 267° (267 keV) at $\alpha = 128^\circ$. The overall phase shift is 93° at $\alpha = 55^\circ$ and 166° at $\alpha = 128^\circ$, with the latter being close to 180° across a resonance that is predicted by theory.
2. At the predicted resonance energy of 117 keV, the corrected cross phase is $\sim 10^\circ$ ($\alpha = 55^\circ$) and $\sim 160^\circ$ ($\alpha = 128^\circ$). These values are in agreement within the margin of error with the theoretical predictions of 0 ($\alpha = 55^\circ$) and 180° ($\alpha = 128^\circ$), which are marked by large circular symbols in Figure 13b.
3. The difference of the cross phase between the near conjugate pitch angles is not exactly 180° . According to Figure 1, particles with a common energy but having conjugate pitch angles should see electric fields that are antisymmetric about the magnetic equator; therefore, the flux perturbations should be exactly in antiphase. The discrepancy between the theoretical expectation and the observations is larger at lower

energies. For example, the difference in the corrected cross phase between the two pitch angles is 124° at 83 keV and 160° at 243 keV.

6. Excitation of P2 Waves Through Bounce Resonance

We noted in Figure 4e that there is a j_{H^+} minimum at ~ 1 keV, which implies that the proton phase space density (denoted F_{H^+}) has a positive energy slope above this energy and forms a bump-on-tail structure. An F_{H^+} with this feature can drive P2 waves unstable through bounce (low-energy) resonance as described in section 2. Previous studies of P2 waves (e.g., Hughes et al., 1978; Liu et al., 2013) reported the presence of this type of F_{H^+} and concluded a causal relationship between the F_{H^+} feature and the waves. Strictly stated, however, these studies examined $\partial F_{H^+} / \partial W|_{\alpha,L}$, not $\partial F_{H^+} / \partial W|_{M,L}$ (the first term on the r.h.s. of equation (4)). These two derivatives are equivalent only when $\partial F_{H^+} / \partial \alpha = 0$, which is not the case as we see below. Moreover, previous studies did not evaluate the second term on the r.h.s. of equation (4). Data from the HOPE instrument allow us to evaluate both terms.

Figures 14a–14c show the W dependence of F_{H^+} that is derived from RBSP-A HOPE data for 1800–1815 UT. The three panels cover α bins centered at the following: 90° (Figure 14a), 54° and its conjugate 126° (Figure 14b), and 18° and its conjugate 162° (Figure 14c). F_{H^+} values for α ($<90^\circ$, solid line) and $180^\circ - \alpha$ (dashed line) are very close to each other as expected. All plots show a positive slope between ~ 3 keV and ~ 10 keV, but the steepness of the slope varies. The vertical red line shown in each of these figures indicates the energy of protons that are in low-energy (bounce) resonance with the given wave at the given pitch angle. As before, the energy was obtained using the Hamlin et al. (1961) approximation for ω_d and ω_b and assuming a wave excited at $L = 5.8$ with a frequency of 10.9 mHz (after a minor correction to the Doppler shift). As ω_d and ω_b depend on α differently, the resonance energy is α dependent. We find that the resonance energy is 5.8 keV for $\alpha = 54^\circ$ and that this energy occurs at the center of the positive slope. At the other pitch angles, in contrast, the resonance energy occurs off the center of the slope. Based on these observations, we assume that bounce resonance occurred at $W = 5.8$ keV and $\alpha = 54^\circ$. Noting that the measured magnetic field had an average magnitude of 155 nT for 1800–1815 UT, we define the magnetic moment of the resonant protons (denoted M_{res}) by $M_{\text{res}} = 5.8$ (keV) $\sin^2(54^\circ) / 155$ (nT).

Figure 14d illustrates how we evaluate $\partial F_{H^+} / \partial W|_{M,L}$ for $M = M_{\text{res}}$ and $L = 5.8$. The curve in this figure was obtained by 2-D interpolation of the observationally defined F_{H^+} at W and α grid point pairs that give $M = M_{\text{res}}$. At 3–10 keV, F_{H^+} increases with W , with the slope (the red dashed line) given by $2.0 \times 10^2 \text{ s}^3 \text{ km}^{-6} \text{ keV}^{-1}$ at the assumed resonance energy of 5.8 keV.

To evaluate the second term on the r.h.s. of equation (4), we first need to determine the value of dL/dW , the ratio between changes in L and W for resonant particles. According to Southwood et al. (1969), the ratio is given by

$$\frac{dL}{dW} = \frac{mL^2}{qB_E \omega R_E^2} \quad (12)$$

where q is the electric charge of the particle and B_E is the magnitude of equatorial magnetic field on the surface of the Earth. For the P2 wave observed at RBSP-A at 1800–1815 UT, we have $L = 5.8$, $m = -200$, $\omega = 0.68$ rad/s. From these, we obtain $dL/dW = -8.1 \times 10^{-2} \text{ keV}^{-1}$.

Figure 14e illustrates how we evaluate $\partial F_{H^+} / \partial L|_{W,M}$. To evaluate the L slope, we computed F_{H^+} in a 20 min data window, which is stepped forward from 1620 to 1840 UT. Similar to the process for Figure 14d, we determine α corresponding to M_{res} in each time step using the measured magnetic field and interpolate F_{H^+} at this α . F_{H^+} increases with L with a slope value of $3.0 \times 10^2 \text{ s}^3 \text{ km}^{-6}$.

By substituting the three numerical factors into equation (4), we find

$$\left. \frac{\partial F_{H^+}}{\partial W} \right|_{M,L} + \left(\frac{dL}{dW} \right) \left. \frac{\partial F_{H^+}}{\partial L} \right|_{W,M} \sim 2.0 \times 10^2 - (8.1 \times 10^{-2}) \times (3.0 \times 10^2) \sim 1.8 \times 10^2 \text{ (s}^3 \text{ km}^{-6} \text{ keV}^{-1}) > 0 \quad (13)$$

This indicates that the second term on the r.h.s. of equation (4) has a negative sign (a stabilizing effect), but its magnitude ($\sim 12\%$ of the first term) is not strong enough to suppress the instability caused by the first term. This result provides strong support to previous studies that suggested that a bump-on-tail energy distribution in the 1–10 keV energy range provides free energy for exciting P2 waves.

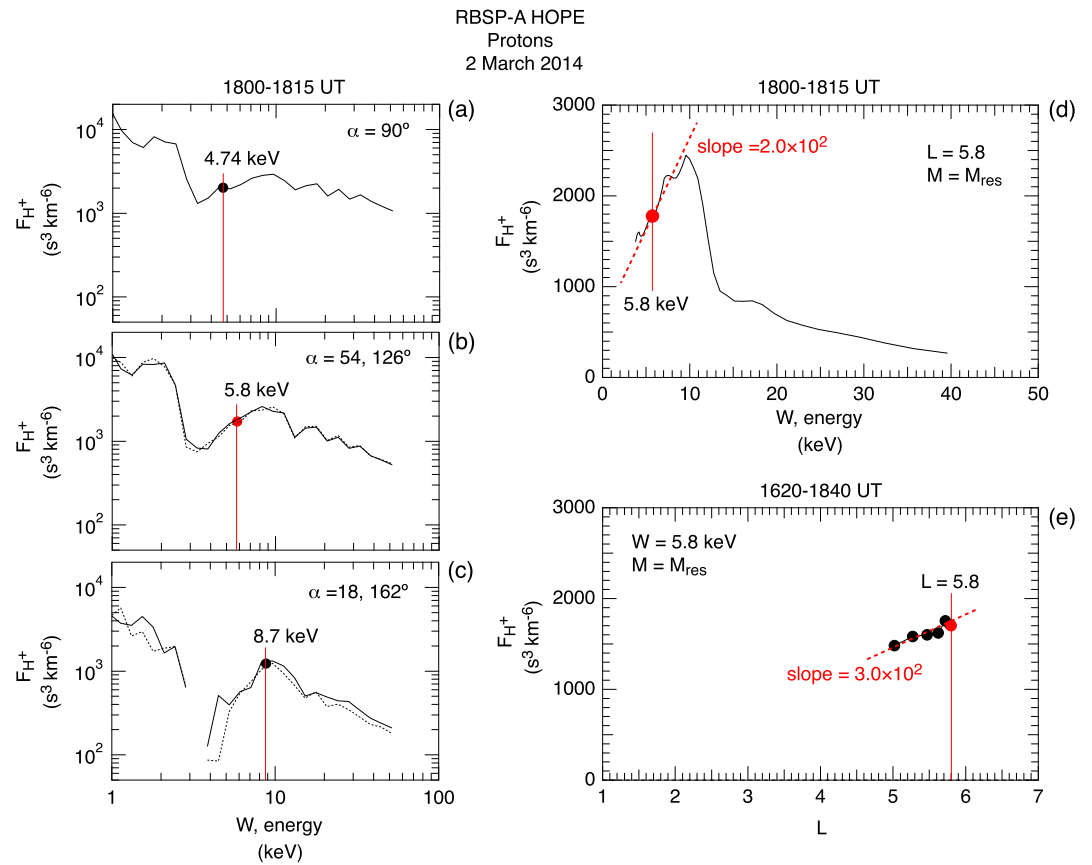


Figure 14. (a–c) Pitch angle-sorted F_{H^+} plotted as a function of energy. The vertical line indicates the energy of protons that are in resonance with the P2 wave described in the text. (d) $F_{H^+}(L = 5.8, M = M_{res})$ plotted as a function of energy. (e) $F_{H^+}(W = 5.8 \text{ keV}, M = M_{res})$ plotted as a function of L .

Figure 15 provides additional evidence that the bounce resonance mechanism is responsible for the P2 waves. Figures 15a and 15b show examples of the energy dependence of F_{H^+} at RBSP-A for $\alpha \sim 50^\circ$. Each example is constructed from counts accumulated in a 20 min interval in the α bin centered on 54° (HOPE) or 50° (RBSPICE). In the first example (Figure 15a, 1620–1640 UT), there are two bumps, with the associated positive slopes logarithmically centered on 0.97 keV (large blue arrow) and 6.6 keV (large red arrow). We refer to these energies as the midslope energies. Following Baddeley et al. (2004), F_{H^+} data points that delimit the slopes are marked by small arrows labeled “min” and “max.” The F_{H^+} values at these energies are denoted F_{H^+min} and F_{H^+max} . In the RBSPICE energy range ($W > 50$ keV), F_{H^+} decreases rapidly with W with no indication of positive slopes. The second example (Figure 15b, 1800–1820 UT) is similar, but the low-energy bump is absent.

We have examined the shape of $F_{H^+}(W)$ in consecutive 20 min segments from 1400 UT to 2300 UT and defined parameters to characterize F_{H^+} as shown in Figures 15c–15f. During this time period, the spacecraft L varied between 2.6 and 5.8 (Figure 15f). Figure 15c shows the midslope energies using symbol colors that match the examples shown in Figures 15a and 15b. A positive slope occurs at both low (blue dots) and high (red dots) energies, but it is more persistent at the high energy. Figure 15d shows the F_{H^+max}/F_{H^+min} ratio, a parameter that defines the strength of the bump. The F_{H^+max}/F_{H^+min} ratio for the high-energy bump is in the range 2–4 and is consistently higher than that for the low-energy bump. Figure 15e shows the proton bounce frequencies ($\omega_b/2\pi$) evaluated at the midslope energies shown in Figure 15c, along with the frequency of the observed P2 waves (f_{p2} , black squares). There is a good match between f_{p2} and the bounce frequency for the high-energy F_{H^+} bump. Therefore, although the type of detailed analysis of F_{H^+} shown in Figure 14 was not conducted for the entire P2 wave event, the results shown in Figure 15 provide strong support of the idea that a bump-on-tail structure of F_{H^+} is causally related to the P2 waves.

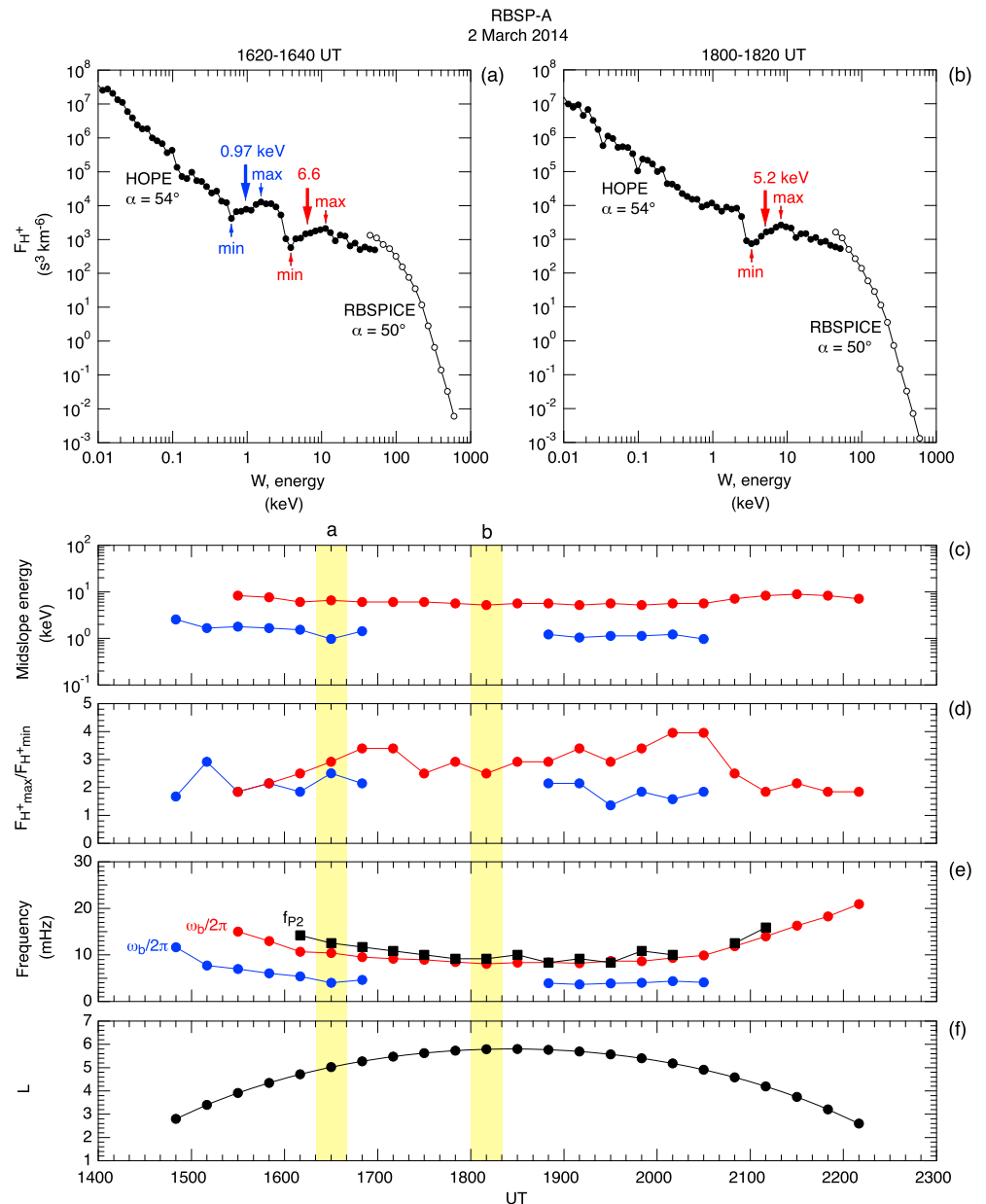


Figure 15. RBSP-A proton data and related parameters for the orbit covering the P2 wave event. (a) F_{H^+} at $\alpha \sim 50^\circ$ averaged over 1620–1640 UT, constructed from HOPE and RBSPICE data. The arrows indicate the energies at the logarithmic midpoints of the F_{H^+} minima and maxima that form positive slopes. (b) Same as panel Figure 15a except for 1800–1820 UT. (c) Proton energies at the logarithmic midpoints of positive energy slopes. The shading indicates the 20 min segments covered in Figures 8a and 8b. (d) Ratios between F_{H^+} maxima and minima that form positive energy slopes. (e) Proton bounce frequencies (red and blue) at the midpoint energies. We assumed $\alpha_{\text{eq}} = 54^\circ$. The data points shown in black are the observed P2 wave frequencies. (f) Proton number density obtained by taking the moment of HOPE data. (g) Proton temperature obtained by taking the moment of HOPE data. (f) L value of the spacecraft.

7. Summary and Discussion

7.1. Azimuthal Wave Number

We used two techniques to determine m . The two-spacecraft phase delay analysis of the magnetic field conducted in 2 min steps indicates that m varied considerably between -100 and -300 with an overall average of ~ -200 . It is difficult to confirm the temporal variability with ion FGR remote sensing because this technique requires long data segments and high particle counts. However, the FGR technique removes the $n\pi$

ambiguity that is intrinsic to the two-spacecraft phase delay analysis and confirms that the P2 waves were propagating westward.

Westward propagation has been commonly reported for poloidal ULF waves detected in the ring current region ($L < 7$) and outer magnetosphere ($L > 7$), including those with strong magnetic field compression (Constantinescu et al., 2009; Le et al., 2017; Lin et al., 1988; Min et al., 2017; Takahashi et al., 1985). This indicates that our P2 waves belong to a family of second-harmonic standing waves generated in the ring current that are predicted by theory (Chen & Hasegawa, 1991; Cheng et al., 1994; Southwood, 1976), although the magnitude of m (~ 200) is higher than previously reported values of 40–160 (Hughes et al., 1979; Le et al., 2017; Lin et al., 1988; Min et al., 2017; Motoba et al., 2015; Schäfer et al., 2008; Takahashi et al., 1985; Takahashi, McEntire, et al., 1990).

7.2. Proton Flux Oscillations

The unambiguous determination of m summarized above made it possible to test the theoretical prediction of the phase of j_{H^+} oscillations relative to the B_v perturbations of the P2 waves detected at the magnetic equator. For a 15 min interval (1800–1815 UT) during which m was steady at ~ -200 , we find that the $\delta B_v - \delta j_{H^+}$ cross phase at the resonance energy predicted by equation (1) is close to 0 or 180° predicted by equation (11). This type of consistency check was never reported before and provides confidence in estimating m from examination of the energy dependence of the $\delta j_{H^+} - \delta B_v$ cross phase (Takahashi, McEntire, et al., 1990).

We note that both the present and the Takahashi, McEntire, et al. (1990) P2 wave events were observed very near the magnetic equator, which made the interpretation of pitch angle dependence of j_{H^+} oscillations easy. It is possible to generalize the technique to determine m from the observed $\delta B_v - \delta j_{H^+}$ cross for observations made away from the equator. In that case, however, equation (11) needs to be modified to incorporate the $\sin \theta_b$ term.

7.3. Instability

Examination of the instability condition (equation (4)) using HOPE data provided convincing evidence that the observed P2 waves were excited by a bump-on-tail structure in F_{H^+} through the bounce resonance ($\omega \sim \omega_b$). The protons that form the positive energy slope have bounce frequencies that are very close to the observed P2 wave frequencies, so the resonance condition is satisfied. Also, the P2 waves are detected when the phase space density ratio $F_{H^+ \max} / F_{H^+ \min}$ (Figure 15d) exceeds a threshold value of ~ 2 . Interestingly, secondary positive energy slopes are seen at lower energies (1–3 keV). However, at these energies, the $F_{H^+ \max} / F_{H^+ \min}$ ratio does not exceed 2, and the bounce frequency does not match the wave frequency. We conclude that the low-energy bump-on-tail distribution does not contribute to the growth of the P2 waves.

This scenario for P2 wave excitation is essentially the same as that discussed previously, for example, by Hughes et al. (1978) and Liu et al. (2013). As these authors have emphasized, the essential conditions for excitation of P2 waves are (a) formation of a bump-on-tail ion (assumed to be proton) energy distribution and (b) the local plasma density that makes the P2 wave frequency close to the bounce frequency of ions at the midslope energy of the bump-on-tail distribution. Singer et al. (1982) was the first to report the relationship between the density structure and P2 wave amplitude, and we now have a good explanation for the density requirement.

Although evidence of the instability through bounce (low-energy) resonance is strong, we cannot exclude the possibility of an instability involving drift-bounce (high-energy) resonance. First of all, there is clear evidence of the resonance in the proton response to the wave field at ~ 100 keV, as detailed in section 5.2. In another P2 wave study reported recently (Min et al., 2017), there was no evidence of a bump-on-tail energy distribution, but there was evidence of drift-bounce resonance instability. It is possible that both bounce resonance and drift-bounce resonance contributed to the excitation of the P2 waves reported here. We are examining the behavior of F_{H^+} at the energy (~ 100 keV) of the drift-bounce resonance and will report the results in a separate publication.

8. Conclusions

We studied a P2 wave event using observations from the RBSP-A and -B spacecraft that were made when they were near noon, very close to the magnetic equator, and maintained a small relative distance. Compared to previous studies of P2 waves, our study is unique in the following aspects:

1. There is unambiguous determination of m and use of that information to confirm the signature of proton drift-bounce resonance ($m\omega_d \sim \omega_b$). Ions satisfying this resonance condition have gyroradii comparable to $2\pi\lambda_\phi$. We showed the need to take FGR effects into account in explaining the behavior of proton flux oscillations observed at ~ 100 keV.
2. There is availability of ion data for assessment of wave excitation through both the bounce resonance ($\omega \sim \omega_b$) and drift-bounce resonance. We presented a detailed analysis of the bounce resonance instability condition and found the instability to be capable of driving P2 waves.

Acknowledgments

Work at JHU/APL was supported by NASA grant NNX14AB97G. Work at Aerospace was supported by RBSP-ECT funding provided by JHU/APL contract 967399 under NASA's prime contract NASS-01072. The work at the New Jersey Institute of Technology was supported by the NASA Van Allen Probes RBSPICE instrument project provided by JHU/APL subcontract 131803 under NASA prime contract NNN06AA01C. K. Takahashi is grateful to Lynn Kistler for her comments on HOPE data. Data used in this work are publicly available from the following sources: magnetic field and electron density data from the RBSP EMFISIS experiment (<http://emfisis.physics.uiowa.edu/>); electric field data from the RBSP EFW experiment (<http://www.space.umn.edu/missions/rbsp/efw-home-university-of-minnesota>); energetic particle data from the RBSP MagEIS experiment (https://www.rbsp-ect.lanl.gov/data_pub/rbspa/mageis/) and the RBSP RBSPICE experiment (<http://rbspice.ftccs.com/Data.html>); *Dst* and *AE* indices generated at the World Data Center Kyoto University (<http://wdc.kugi.kyoto-u.ac.jp/dstdir/>).

References

- Ali, A. F., Malaspina, D. M., Elkington, S. R., Jaynes, A. N., Chan, A. A., Wygant, J., & Kletzing, C. A. (2016). Electric and magnetic radial diffusion coefficients using the Van Allen probes data. *Journal of Geophysical Research: Space Physics*, 121, 9586–9607. <https://doi.org/10.1002/2016JA023002>
- Anderson, B. J., Engebretson, M. J., Rounds, S. P., Zanetti, L. J., & Potemra, T. A. (1990). A statistical study of Pc 3–5 pulsations observed by the AMPTE/CCE Magnetic Fields Experiment, 1. Occurrence distributions. *Journal of Geophysical Research*, 95(A7), 10,495–10,523. <https://doi.org/10.1029/JA095IA07p10495>
- Arthur, C. W., & McPherron, R. L. (1981). The statistical character of Pc4 magnetic pulsations at synchronous orbit. *Journal of Geophysical Research*, 86(A3), 1325. <https://doi.org/10.1029/JA086IA03p01325>
- Baddeley, L. J., Yeoman, T. K., Wright, D. M., Trattner, K. J., & Kellet, B. J. (2004). A statistical study of unstable particle populations in the global ring current and their relation to the generation of high m ULF waves. *Annales Geophysicae*, 22(12), 4229–4241. <https://doi.org/10.5194/angeo-24-3027-2006>
- Bendat, J. S., & Piersol, A. G. (1971). *Random data: Analysis and measurement procedures*. New York: John Wiley.
- Blake, J. B., Carranza, P. A., Claudepierre, S. G., Clemmons, J. H., Crain, W. R., Dotan, Y., ... Zakrzewski, M. P. (2013). The Magnetic Electron Ion Spectrometer (MagEIS) instruments aboard the Radiation Belt Storm Probes (RBSP) spacecraft. *Space Science Reviews*, 179(1–4), 383–421. <https://doi.org/10.1007/s11214-013-9991-8>
- Chan, A. A. (1991). Interaction of energetic ring current protons with magnetospheric hydromagnetic waves (PhD Thesis), Princeton University, Princeton, NJ.
- Chen, L., & Hasegawa, A. (1988). On magnetospheric hydromagnetic waves excited by energetic ring-current particles. *Journal of Geophysical Research*, 93(A8), 8763. <https://doi.org/10.1029/JA093JA08p08763>
- Chen, L., & Hasegawa, A. (1991). Kinetic theory of geomagnetic pulsations: 1. Internal excitations by energetic particles. *Journal of Geophysical Research*, 96(A2), 1503–1512. <https://doi.org/10.1029/90JA02346>
- Chen, L., & Hasegawa, A. (1994). Kinetic theory of geomagnetic pulsations: 2. Ion flux modulations by transverse waves. *Journal of Geophysical Research*, 99(A1), 179. <https://doi.org/10.1029/93JA02774>
- Cheng, C. Z. (1991). A kinetic-magnetohydrodynamic model for low-frequency phenomena. *Journal of Geophysical Research*, 96(A12), 21,159–21,171. <https://doi.org/10.1029/91JA01981>
- Cheng, C. Z., & Qian, Q. (1994). Theory of ballooning-mirror instabilities for anisotropic pressure plasmas in the magnetosphere. *Journal of Geophysical Research*, 99(A6), 11,193–11,209. <https://doi.org/10.1029/94JA00657>
- Cheng, C. Z., Qian, Q., Takahashi, K., & Lui, A. T. Y. (1994). Ballooning-mirror instability and internally driven Pc 4–5 wave events. *Journal of Geomagnetism and Geoelectricity*, 46(11), 997–1009. <https://doi.org/10.5636/jgg.46.997>
- Chisham, G. (1996). Giant pulsations: An explanation for their rarity and occurrence during geomagnetically quiet times. *Journal of Geophysical Research*, 101(A11), 24,755–24,763. <https://doi.org/10.1029/96JA02540>
- Constantinescu, O. D., Glassmeier, K. H., Plaschke, F., Auster, U., Angelopoulos, V., Baumjohann, W., ... Narita, Y. (2009). THEMIS observations of duskside compressional Pc5 waves. *Journal of Geophysical Research*, 114, A00C25. <https://doi.org/10.1029/2008JA013519>
- Cummings, W. D., O'Sullivan, R. J., & Coleman, P. J. Jr (1969). Standing Alfvén waves in the magnetosphere. *Journal of Geophysical Research*, 74(3), 778–793. <https://doi.org/10.1029/JA074i003p00778>
- Dai, L., Takahashi, K., Wygant, J. R., Chen, L., Bonnell, J., Cattell, C. A., ... Spence, H. E. (2013). Excitation of poloidal standing Alfvén waves through drift resonance wave-particle interaction. *Geophysical Research Letters*, 40, 4127–4132. <https://doi.org/10.1002/grl.50800>
- Ejiri, M., Hoffman, R. A., & Smith, P. H. (1980). Energetic particle penetrations into the inner magnetosphere. *Journal of Geophysical Research*, 85(A2), 653–663. <https://doi.org/10.1029/JA085IA02p00653>
- Engebretson, M. J., Murr, D. L., Erickson, K. N., Strangeway, R. J., Klumpp, D. M., Fuselier, S. A., ... Potemra, T. A. (1992). The spatial extent of radial magnetic pulsation events observed in the dayside near synchronous orbit. *Journal of Geophysical Research*, 97(A9), 13,741–13,758. <https://doi.org/10.1029/92JA00992>
- Ferradas, C. P., Zhang, J. C., Spence, H. E., Kistler, L. M., Larsen, B. A., Reeves, G., ... Funsten, H. (2016). Ion nose spectral structures observed by the Van Allen Probes. *Journal of Geophysical Research*, 121, 12,025–12,046. <https://doi.org/10.1002/2016JA022942>
- Funsten, H. O., Skoug, R. M., Guthrie, A. A., MacDonald, E. A., Baldonado, J. R., Harper, R. W., ... Chen, J. (2013). Helium, oxygen, proton, and electron (HOPE) mass spectrometer for the Radiation Belt Storm Probes mission. *Space Science Reviews*, 179(1–4), 423–484. <https://doi.org/10.1007/s11214-013-9968-7>
- Green, C. A. (1976). The longitudinal phase variation of mid-latitude Pc3–4 micropulsations. *Planetary and Space Science*, 24(1), 79–85. [https://doi.org/10.1016/0032-0633\(76\)90064-7](https://doi.org/10.1016/0032-0633(76)90064-7)
- Hamlin, D. A., Karplus, R., Vik, R. C., & Watson, K. M. (1961). Mirror and azimuthal drift frequencies for geomagnetically trapped particles. *Journal of Geophysical Research*, 66(1), 1–4. <https://doi.org/10.1029/JZ066i001p00001>
- Hughes, W. J., & Grard, R. J. L. (1984). A second harmonic geomagnetic field line resonance at the inner edge of the plasma sheet: GEOS 1, ISEE 1, and ISEE 2 observations. *Journal of Geophysical Research*, 89(A5), 2755–2764. <https://doi.org/10.1029/JA089IA05p02755>
- Hughes, W. J., & Southwood, D. J. (1976). The screening of micropulsation signals by the atmosphere and ionosphere. *Journal of Geophysical Research*, 81(19), 3234–3240. <https://doi.org/10.1029/JA081i019p03234>
- Hughes, W. J., McPherron, R. I., Barfield, J. N., & Mauk, B. H. (1979). A compressional Pc4 pulsation observed by three satellites in geostationary orbit near local midnight. *Planetary and Space Science*, 27(6), 821–840. [https://doi.org/10.1016/0032-0633\(79\)90010-2](https://doi.org/10.1016/0032-0633(79)90010-2)
- Hughes, W. J., Southwood, D. J., Mauk, B., McPherron, R. L., & Barfield, J. N. (1978). Alfvén waves generated by an inverted plasma energy distribution. *Nature*, 275(5675), 43–45. <https://doi.org/10.1038/275043a0>
- Kivelson, M. G., & Southwood, D. J. (1983). Charged particle behavior in low-frequency geomagnetic pulsations: 3. Spin phase dependence. *Journal of Geophysical Research*, 88(A1), 174–182. <https://doi.org/10.1029/JA088IA01p00174>

- Kivelson, M. G., & Southwood, D. J. (1986). Coupling of global magnetospheric MHD eigenmodes to field line resonances. *Journal of Geophysical Research*, 91(A4), 4345–4351. <https://doi.org/10.1029/JA091iA04p04345>
- Kletzing, C. A., Kurth, W. S., Acuna, M., MacDowall, R. J., Torbert, R. B., Averkamp, T., ... Tyler, J. (2013). The electric and magnetic field instrument suite and integrated science (EMFISIS) on RBSP. *Space Science Reviews*, 179(1–4), 127–181. <https://doi.org/10.1007/s11214-013-9993-6>
- Kokubun, S., Erickson, K. N., Fritz, T. A., & McPherron, R. L. (1989). Local time asymmetry of Pc-4–5 pulsations and associated particle modulations at synchronous orbit. *Journal of Geophysical Research*, 94(A6), 6607–6625. <https://doi.org/10.1029/JA094iA06p06607>
- Korotova, G. I., Sibeck, D. G., Takahashi, K., Dai, L., Spence, H. E., Kletzing, C. A., ... Redmon, R. J. (2015). Van Allen Probe observations of drift-bounce resonances with Pc 4 pulsations and wave-particle interactions in the pre-midnight inner magnetosphere. *Annales Geophysicae*, 33(8), 955–964. <https://doi.org/10.5194/angeo-33-955-2015>
- Korotova, G., Sibeck, D., Engebretson, M., Wygant, J., Thaller, S., Spence, H., ... Redmon, R. (2016). Multipoint spacecraft observations of long-lasting poloidal Pc4 pulsations in the dayside magnetosphere on 1–2, May 2014. *Annales Geophysicae*, 34(11), 985–998. <https://doi.org/10.5194/angeo-34-985-2016>
- Kurth, W. S., De Pascuale, S., Faden, J. B., Kletzing, C. A., Hospodarsky, G. B., Thaller, S., & Wygant, J. R. (2015). Electron densities inferred from plasma wave spectra obtained by the Waves instrument on Van Allen Probes. *Journal of Geophysical Research: Space Physics*, 120, 904–914. <https://doi.org/10.1002/2014JA020857>
- Le, G., Chi, P. J., Strangeway, R. J., Russell, C. T., Slavin, J. A., Takahashi, K., ... Torbert, R. B. (2017). Global observations of magnetospheric high-m poloidal waves during the 22 June 2015 magnetic storm. *Geophysical Research Letters*, 44, 3456–3464. <https://doi.org/10.1002/2017GL073048>
- Lin, N., McPherron, R. L., Kivelson, M. G., & Williams, D. J. (1988). An unambiguous determination of the propagation of a compressional Pc 5 wave. *Journal of Geophysical Research*, 93(A6), 5601–5612. <https://doi.org/10.1029/JA093iA06p05601>
- Liu, W., Cao, J. B., Li, X., Sarris, T. E., Zong, Q. G., Hartinger, M., ... Angelopoulos, V. (2013). Poloidal ULF wave observed in the plasmasphere boundary layer. *Journal of Geophysical Research: Space Physics*, 118, 4298–4307. <https://doi.org/10.1002/jgra.50427>
- Liu, W., Tu, W., Li, X., Sarris, T., Khotyaintsev, Y., Fu, H., ... Shi, Q. (2016). On the calculation of electric diffusion coefficient of radiation belt electrons with in situ electric field measurements by THEMIS. *Geophysical Research Letters*, 43, 1023–1030. <https://doi.org/10.1002/2015gl067398>
- Mauk, B. H., Fox, N. J., Kanekal, S. G., Kessel, R. L., Sibeck, D. G., & Ukhorskiy, A. (2012). Science objectives and rationale for the Radiation Belt Storm Probes mission. *Space Science Reviews*, 179(1–4), 3–27. <https://doi.org/10.1007/s11214-012-9908-y>
- Min, K., Takahashi, K., Ukhorskiy, A. Y., Manweiler, J. W., Spence, H. E., Singer, H. J., ... Cohen, R. J. (2017). Second harmonic poloidal waves observed by Van Allen Probes in the dusk-midnight sector. *Journal of Geophysical Research: Space Physics*, 122, 3013–3039. <https://doi.org/10.1002/2016JA023770>
- Mitchell, D. G., Lanzerotti, L. J., Kim, C. K., Stokes, M., Ho, G., Cooper, S., ... Kerem, S. (2013). Radiation belt storm probes ion composition experiment (RBSPICE). *Space Science Reviews*, 179(1–4), 263–308. <https://doi.org/10.1007/s11214-013-9965-x>
- Motoba, T., Takahashi, K., Rodriguez, J. V., & Russell, C. T. (2015). Giant pulsations on the afternoonside: Geostationary satellite and ground observations. *Journal of Geophysical Research: Space Physics*, 120, 8350–8367. <https://doi.org/10.1002/2015JA021592>
- Radoski, H. R. (1967). Highly asymmetric MHD resonances: The guided poloidal mode. *Journal of Geophysical Research*, 72(15), 4026–4027. <https://doi.org/10.1029/JZ072i015p04026>
- Schäfer, S., Glassmeier, K. H., Eriksson, P. T. I., Mager, P. N., Pierrard, V., Fornaçon, K. H., & Blomberg, L. G. (2008). Spatio-temporal structure of a poloidal Alfvén wave detected by Cluster adjacent to the dayside plasmopause. *Annales Geophysicae*, 26(7), 1805–1817. <https://doi.org/10.5194/angeo-26-1805-2008>
- Singer, H. J., Hughes, W. J., & Russell, C. T. (1982). Standing hydromagnetic waves observed by ISEE 1 and 2: Radial extent and harmonic. *Journal of Geophysical Research*, 87(A5), 3519–3529. <https://doi.org/10.1029/JA087iA05p03519>
- Southwood, D. J. (1976). A general approach to low-frequency instability in the ring current plasma. *Journal of Geophysical Research*, 81(19), 3340–3348. <https://doi.org/10.1029/JA081i019p03340>
- Southwood, D. J., & Hughes, W. J. (1983). Theory of hydromagnetic waves in the magnetosphere. *Space Science Reviews*, 35(4), 301–366. <https://doi.org/10.1007/bf00169231>
- Southwood, D. J., & Kivelson, M. G. (1981). Charged particle behavior in low-frequency geomagnetic pulsations 1. Transverse waves. *Journal of Geophysical Research*, 86(A7), 5643–5655. <https://doi.org/10.1029/JA086iA07p05643>
- Southwood, D. J., & Kivelson, M. G. (1982). Charged particle behavior in low-frequency geomagnetic pulsations, 2. Graphical approach. *Journal of Geophysical Research*, 87(A3), 1707–1710. <https://doi.org/10.1029/JA087iA03p01707>
- Southwood, D. J., Dungey, J. W., & Etherington, R. J. (1969). Bounce resonant interaction between pulsations and trapped particles. *Planetary and Space Science*, 17(3), 349–361. [https://doi.org/10.1016/0032-0633\(69\)90068-3](https://doi.org/10.1016/0032-0633(69)90068-3)
- Su, S. Y., Konradi, A., & Fritz, T. A. (1977). On propagation direction of ring current proton ULF waves observed by ATS 6 at 6.6 R_E . *Journal of Geophysical Research*, 82(13), 1859–1868. <https://doi.org/10.1029/JA082i013p01859>
- Su, S. Y., Konradi, A., & Fritz, T. A. (1979). On energy dependent modulation of the ULF ion flux oscillations observed at small pitch angles. *Journal of Geophysical Research*, 84(A11), 6510–6516. <https://doi.org/10.1029/JA084iA11p06510>
- Takahashi, K., & Anderson, B. J. (1992). Distribution of ULF energy ($f < 80$ mHz) in the inner magnetosphere: A statistical analysis of AMPTE CCE magnetic field data. *Journal of Geophysical Research*, 97(A7), 10,751–10,773. <https://doi.org/10.1029/92JA00328>
- Takahashi, K., & McPherron, R. L. (1984). Standing hydromagnetic oscillations in the magnetosphere. *Planetary and Space Science*, 32(11), 1343–1359. [https://doi.org/10.1016/0032-0633\(84\)90078-3](https://doi.org/10.1016/0032-0633(84)90078-3)
- Takahashi, K., Cheng, C. Z., McEntire, R. W., & Kistler, L. M. (1990). Observation and theory of Pc5 waves with harmonically related transverse and compressional components. *Journal of Geophysical Research*, 95(A2), 977–989. <https://doi.org/10.1029/JA095iA02p0977>
- Takahashi, K., Denton, R. E., Kurth, W., Kletzing, C., Wygant, J., Bonnell, J., ... MacDowall, R. (2015). Externally driven plasmaspheric ULF waves observed by the Van Allen Probes. *Journal of Geophysical Research: Space Physics*, 120, 526–552. <https://doi.org/10.1002/2014JA020373>
- Takahashi, K., Hartinger, M. D., Malaspina, D. M., Smith, C. W., Koga, K., Singer, H. J., ... Yoshikawa, A. (2016). Propagation of ULF waves from the upstream region to the midnight sector of the inner magnetosphere. *Journal of Geophysical Research: Space Physics*, 121, 8428–8447. <https://doi.org/10.1002/2016JA022958>
- Takahashi, K., Higbie, P. R., & Baker, D. N. (1985). Azimuthal propagation and frequency characteristic of compressional Pc 5 waves observed at geostationary orbit. *Journal of Geophysical Research*, 90(A2), 1473–1485. <https://doi.org/10.1029/JA090iA02p01473>
- Takahashi, K., McEntire, R. W., Lui, A. T. Y., & Potemra, T. A. (1990). Ion flux oscillations associated with a radially polarized transverse Pc 5 magnetic pulsation. *Journal of Geophysical Research*, 95(A4), 3717–3731. <https://doi.org/10.1029/JA095iA04p03717>

- Takahashi, K., Sato, N., Warnecke, J., Lühr, H., Spence, H. E., & Tonegawa, Y. (1992). On the standing wave mode of giant pulsations. *Journal of Geophysical Research*, *97*(A7), 10,717–10,732. <https://doi.org/10.1029/92JA00382>
- Takahashi, K., Waters, C., Glassmeier, K.-H., Kletzing, C. A., Kurth, W. S., & Smith, C. W. (2015). Multifrequency compressional magnetic field oscillations and their relation to multiharmonic toroidal mode standing Alfvén waves. *Journal of Geophysical Research: Space Physics*, *120*, 10,384–10,403. <https://doi.org/10.1002/2015JA021780>
- Tsyganenko, N. A. (1989). A magnetospheric magnetic field model with a warped tail current sheet. *Planetary and Space Science*, *37*(1), 5–20. [https://doi.org/10.1016/0032-0633\(89\)90066-4](https://doi.org/10.1016/0032-0633(89)90066-4)
- Wilson, M. E., Yeoman, T. K., Baddeley, L. J., & Kellet, B. J. (2006). A Statistical investigation of the invariant latitude dependence of unstable magnetospheric ion populations in relation to high m ULF wave generation. *Annales Geophysicae*, *24*(11), 3027–3040. <https://doi.org/10.5194/angeo-24-3027-2006>
- Wygant, J. R., Bonnell, J. W., Goetz, K., Ergun, R. E., Mozer, F. S., Bale, S. D., ... Tao, J. B. (2013). The electric field and waves instruments on the radiation belt storm probes mission. *Space Science Reviews*, *179*(1–4), 183–220. <https://doi.org/10.1007/s11214-013-0013-7>
- Zhu, X., & Kivelson, M. G. (1991). Compressional ULF waves in the outer magnetosphere: 1. Statistical study. *Journal of Geophysical Research*, *96*(A11), 19,451–19,467. <https://doi.org/10.1029/91JA01860>